DLR-IB-AE-GO-2017-30

Review of a Method for Local Damping Identification in the Low- and Mid-Frequency Range Based on a Finite Element Model

Studienarbeit

Martin Tang

Deutsches Zentrum
DLR für Luft- und Raumfahrt

Dokumenteigenschaften

Titel	Review of a Method for Local Damping Identification in the Low- and Mid-Frequency Range Based on a Finite Element Model
Betreff	Aeroelastische Modellierung
Institut	Aeroelastik
Erstellt von	Martin Tang
Beteiligte	Dr. Marco Norambuena
	Dr. Jörn Biedermann
	Dr. René Winter
Geprüft von	Dr. Marc Böswald
Freigabe von	Prof. Dr. Lorenz Tichy
Datum	03.04.17
Version	1.0
Dateipfad	DLR-IB-AE-GO-2017-30.pdf

Institutsleiter:

Prof. Dr.-Ing. L. Tichy

Autor:

M. Tang

Abteilungsleiter:

Dr.-Ing. M. Böswald

Gruppenleiter:

Dr. rer. nat. R. Winter

Abstract

Passenger demand for enhanced cabin comfort have made cabin noise to an important factor. The damping behaviour of the cabin must be understood in order to predict noise emission. Due to the high modal density and overlap, state-of-the-art methods are not able to accurately identify damping in the mid- and high-frequency range. However, these frequency ranges are relevant in the field of acoustics.
2016 a method was proposed for local damping identification, which was applied to an aircraft fuselage. A spatial distribution of damping was calculated in the low-frequency range. This calculated damping distribution supports damping modelling in numerical models in order to achieve more accurate results in the low-frequency range. This method needs to be extended to the mid-frequency range for accurate predictions of cabin noise.
The present work reviews and tests this method with numerical examples. A plate representing a simplified aircraft fuselage skin field is taken as model. Three test cases were defined to test the method. Homogeneous structural damping is applied to the first case. In the second case a patch with higher structural damping is added. The patch is replaced with viscoelastic material in the third case.
The applied damping distribution in the first case is homogeneous and in the second and third case the patch should show a different damping behaviour than the rest of the plate. The calculated damping distribution in each case, however, does not reflect the applied damping distribution.
It is shown that the calculated damping distributions relate to the mode shapes. Especially the nodal lines and closely spaced eigenfrequencies yield a calculated distribution of damping, which is not driven by physics. The interaction between closely spaced eigenfrequencies disturb the decay of the vibration. Thus the damping ratio is identified wrongly.
Finally the damping identification in the mid-frequency range is tested. Instead of a local damping identification per frequency, a global equivalent identification in a frequency band is investigated. Therefore, the calculated damping ratio is averaged in frequency and in space, so the measurement of several points is necessary. The calculated damping ratios are close to the values applied.

Kurzfassung

Kabinenlärm in Flugzeugen nimmt eine immer wichtigere Rolle ein, da die Nachfrage nach erhöhtem Kabinenkomfort immer mehr zunimmt. Es ist erforderlich das Dämpfungsverhalten der Flugzeugkabine zu verstehen, um eine Vorhersage des Kabinenlärms zu treffen. Aufgrund der hohen modalen Dichte und Überlappung sind aktuelle Methoden nicht in der Lage, das Dämpfungsverhalten im mittleren und hohen Frequenzbereich zu identifizieren. Diese Frequenzbereiche sind in der Akustik jedoch von besonderer Bedeutung.
2016 wurde eine Methode vorgestellt, um lokales Dämpfungsverhalten zu identifizieren. Diese Methode wurde auf eine Flugzeugkabine angewandt. Im unteren Frequenzbereich wurde eine räumliche Dämpfungsverteilung berechnet. Mit Hilfe dieser Verteilung ist es möglich, die Dämpfung im unteren Frequenzbereich in numerischen Modellen besser nachzubilden. Eine Erweiterung dieser Methode auf den höheren Frequenzbereich ist notwendig für die Lärmvorhersage.
In der vorliegenden Arbeit wird die vorgestellte Methode mit numerischen Modellen untersucht. Drei Testfälle sind definiert, um die Methode zu validieren: Erstens wird eine homogene strukturelle Dämpfungsverteilung vorgegeben, zweitens wird die strukturelle Dämpfung lokal erhöht und drittens wird lokal ein viskoelastisches Material eingesetzt. Die Dämpfungsverteilung im ersten Fall ist homogen und im zweiten und dritten Fall sollte lokal ein anderes Dämpfungsverhalten auftreten. Die von der Methode berechneten Dämpfungsverteilungen geben diese vorgegebenen Dämpfungsverteilungen aber nicht wieder. Es wird gezeigt, dass die berechneten Dämpfungsverteilungen von der Schwingungsform abhängig sind. Aufgrund von Schwingungsknoten und dicht beieinanderliegenden Eigenfrequenzen werden Dämpfungsverteilungen berechnet, die nicht von physikalischer Natur sind. Durch die Wechselwirkung zweier dicht beieinanderliegende Eigenfrequenzen wird das Abklingen der Schwingung falsch abgeschätzt.
Zudem wird die Dämpfungsidentifikation im mittleren Frequenzbereich geprüft. Anstelle einer lokalen Dämpfungsidentifikation wird eine globale äquivalente Identifikation in einem Frequenzband untersucht. Das Dämpfungsmaß ist also räumlich und im Frequenzband gemittelt. Für die räumliche Mittelung ist die Messung an mehreren Punkten erforderlich. Die berechneten Dämpfungsmaße stimmen gut mit den vorgegebenen Werten überein.

Contents

List of Symbols

A	Amplitude
D	Damping Ratio
$[D]$	Damping Matrix
E	Young's Modulus
f	Frequency
Δf	Frequency Resolution in Frequency Domain
$\{F\}$	Force Vector
g	Structural Damping Parameter
j	Imaginary Number
$[K]$	Stiffness Matrix
$[M]$	Mass Matrix
N	Number of Modes
$\{x\}$	Physical Coordinate
$\{q\}$	Modal Coordinate
$\{Q\}$	Generalised Force
t	Time
T	Total Measurement Time
T_{60}	Reverberation Time
α,β	Parameters for Rayleigh Damping
ε	Strain
ν	Poisson Ratio
ω	Eigenfrequency in Radians
Ω	Frequency of Applied Force
$\{\varphi\}$	Eigenvector
$[\Phi]$	Matrix with Columnwise Eigenvectors
ψ	Phase Shift
ρ	Density
σ	Stress

List of Acronyms

ACARE	The Advisory Council for Aviation Research and Innovation in Europe
DoF	Degree of Freedom
EMA	Experimental Modal Analysis
FEM	Finite Element Method
FRF	Frequency Response Function
MDoF	Multiple Degree of Freedom
ODE	Ordinary Differential Equation
PDE	Partial Differential Equation
SDoF	Single Degree of Freedom
SEA	Statistical Energy Analysis
STFT	Short Time Fourier Transform

1. Introduction

The driving mechanisms for aircraft development are: more affordable, safer, cleaner and quieter aircraft. The focus lies on cleaner aircraft, due to the increasing environmental consciousness of the society. To achieve cleaner aircraft and therefore reduce pollution, new propulsion concepts and lighter structures are required. A promising new propulsion concept is the modern turbo-prop engine. This propulsion concept, however, has drawbacks in engine noise and noise transmission into the aircraft cabin. Light structures will amplify noise transmission. The two goals of cleaner aircraft and reducing cabin noise are contradicting, hence the noise reduction in an aircraft cabin is very challenging. One objective of the Advisory Council for Aviation Research and Innovation in Europe (ACARE) is the reduction of cabin noise to the noise of a car travelling at motorway speed until 2020 [1].

Improved noise characteristics with light structures can only be achieved if the driving mechanisms for noise transmission are understood. To get a deep insight into noise transmission the behaviour of damping of the structure is essential. This work was conducted within the vibroacoustic team in the Structural Dynamics and System Identification department of the Institute of Aeroelasticity at DLR and focuses on damping identification.

For vibroacoustic applications, the relevant frequency range of the tonal excitations of the turbo-prop engines is the so-called mid-frequency range. In the high-frequency range, turbulent boundary layer excitation and jet noise can be predicted with statistical approaches like Statistical Energy Analysis (SEA). In this approach, the mechanical behaviour is averaged over a wide frequency range, so detailed knowledge of the structural behaviour is not necessary, i.e. mode shapes and eigenfrequencies are not needed. Whereas, Experimental Modal Analysis (EMA) of a dynamic structure to identify the mechanical properties is only applicable in the low-frequency range, because the resonances of the structure are distinguishable and distributed in the frequency domain. Also deterministic numerical methods, e.g. Finite Element Method (FEM), are suitable in the low-frequency range. The gap between the low-frequency methods and the high-frequency methods is called *the mid-frequency problem* [7]. Current research is done to extend FEM to the higher frequencies or extend SEA to the lower frequencies.

In order to predict the dynamic response of a structure in the mid- to high-frequency range with FEM, model assumptions, structural details and the nodal resolution must be reasonably accurate. However, it is difficult to model the structure in such a detail. In the mid- to high-frequency range every component of the structure contributes to the structural dynamic behaviour like screws, rivets and imperfections of the structure. Also the damping of the structure is often unknown and in case of numerical models, it is based on estimates and assumptions. Even nowadays there is no satisfactory theory to model damping. The damping is approximated with some non-physical models. Often a constant damping over the whole frequency range is assumed. If the mass, stiffness and especially the damping could be modelled accurately, the FEM would be able to predict the dynamic behaviour of the structure properly.

Norambuena et al. [12] proposed the Local Damping Identification Method based on the reverberation time from building acoustics. This method calculates a local damping distribution of the structure. Knowing the local damping distribution of the structure, an accurate damping can be modelled. This improves the prediction of the dynamic response of a structure, thus it is possible to extend the validity into the mid-frequency range. The damping distribution reveals the components of the structure, where the energy dissipation is taking place. This information will help to improve the physical damping modelling.

In the first part of this work, the theoretical background is outlined. Fundamentals of structural dynamics are presented. A continuous system is discretised with FEM. The basic equations of those discretised systems are derived and the modal space is explained. Finally, the new method for damping identification is presented. In the second part the calculated local damping distributions are reviewed. The method is used on a FE Model, namely a basic plate. The applied damping parameters are varied. First a homogeneous distribution of structural damping is applied. Then, the damping is localised on a specific patch. Finally viscoelastic damping is applied to a local part of the plate, which is the most realistic damping model of all cases. In the third part this Local Damping Identification Method is used to identify a global equivalent damping value in the mid-frequency range in a frequency band. The modal density is high, so several modes in one frequency band are inevitable. In a simple theoretical test case the influence of three modes in one frequency band is analysed. After this theoretical test case the method is applied to the FE Model in order to identify global equivalent damping ratios in the mid-frequencies. The calculated global equivalent damping ratios are implemented in a FE Model. This new implemented FE Model is then compared with the original one.

2. Theoretical Background

This chapter presents the theoretical background for the following chapters. It is shown how the FEM discretises continuous systems into Multiple Degree of Freedom (MDoF) Systems. These equations can be transformed to an eigenvalue problem. This introduces the modal space and allows the separation into multiple eigenfrequencies and corresponding mode shapes. The MDoF equations are decoupled into multiple Single Degree of Freedom (SDoF) equations. Additionally, common damping models are presented. Furthermore, the Local Damping Identification Method, which is a frequency and time domain hybrid, is explained.

2.1. Structural Dynamics

The first step of setting up a simulation is creating a physical model of the problem. Then the equations are derived, which is called the mathematical model. The solution of this mathematical model is interpreted in physical terms again. The mathematical models of continuous structures are partial differential equations (PDE). PDEs are difficult to handle, so analytical solutions are only available for simple problems. This section shows how those PDEs are simplified.

2.1.1. Time Domain

The PDEs in structural dynamics are formulated in time domain, i.e. the variables are time dependent. FEM is a numerical method to solve PDEs. This method originated from structural mechanics and is recognised as a useful tool. Commercial solutions are widely available and used. The PDE and the Geometry of the problem are discretised, in order to approximate the solution of the problem.

In structural dynamics the FEM discretises the structure in a finite number of degrees of

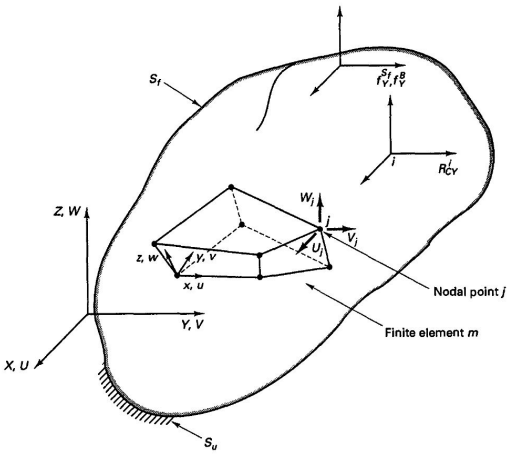

Figure 2.1.: **General three-dimensional body with an 8-node three-dimensional element [3]**

freedom (DoF), in order to approximate the dynamic responses of the structure. This is the geometrical approximation of the structure. Figure 2.1 shows a finite element in a structure. The element is a 3D volume element and consists of 8 connected nodes, which are illustrated as black dots. Many assembled elements approximate the structure. Each Node has six DoF: three translational and three rotational DoF. Many elements with many formulations are available. There are, for instance beam elements, shell elements or volume elements.

The PDE is approximated with so-called shape-functions. These shape-functions are commonly polynomials, since they are easy to handle. The type of element, which is chosen to predict the dynamic response at the discrete nodes, specifies the used shape-functions for the approximation. The element shown in Fig. 2.1 is also known as brick element. It is a 3D volume element with linear shape-functions. The rotations are not defined for this element.

An energy approach is used to derive a set of linear equations. The coefficients of the shape-functions are chosen to minimise the total energy, in order to approximate the correct solution. Starting from the differential equation, the mass matrix and the stiffness matrix are calculated. The damping matrix is chosen arbitrarily. With the help of FEM, the PDEs are simplified to a coupled set of ordinary differential equations (ODE) in time domain, also known as the equation of motion [3]:

$$[M]\{\ddot{x}\} + [D]\{\dot{x}\} + [K]\{x\} = \{F\}, \tag{2.1}$$

where $[M]$ is the mass matrix, $[D]$ is the damping matrix and $[K]$ is the stiffness matrix. $\{F\}$ is the load vector and $\{x\}$ is the displacement vector.

2.1.2. Frequency Domain

Section 2.1.1 shows that continuous structures can be simplified to a discrete system. This is also referred as MDoF System. These equations are easier to handle. Assuming that the applied force is harmonic and can be described by a complex exponential function $F(j\Omega) = \hat{F}e^{j\Omega t}$, the system will also respond in a harmonic manner. The response will be $X(j\Omega) = \hat{X}e^{j\Omega t}$. Equation (2.1) can be transformed into

$$\left(-\Omega^2 [M] + j\Omega [D] + [K]\right) \left\{\hat{X}\right\} = \left\{\hat{F}\right\}. \tag{2.2}$$

This is called frequency domain, since the equation is not dependent on time anymore, but dependent on the frequency only.

2.1.3. Modal Space

If Eq. (2.2) is set to zero and the damping is neglected, the eigenvalue problem for dynamic systems can be formulated. The eigenvalues ω are the eigenfrequencies in radians per second and the eigenvectors $\{\varphi\}$ are the mode shapes of the structure:

$$\left(-\omega^2 [M] + [K]\right) \{\varphi\} = \{0\}. \tag{2.3}$$

A set of mode shape and eigenfrequency is called mode. The mode shapes $\{\varphi\}$ can diagonalise the mass matrix and the stiffness matrix, since they are orthogonal to those two matrices. Mathematically, this means that the set of coupled ODEs can be decoupled into a set of independent ODEs. In order to decouple the equation, the vector $\{x\} = [\phi]\{q\}$ is introduced. $\{q\}$ is called modal coordinates and $[\phi]$ is the matrix with columnwise eigenvectors of the system. The equation has to be premultiplied with $[\phi]^\mathsf{T}$ as well. With the eigenvectors the equation of motion (2.1) can be transformed into modal space:

$$[\phi]^\mathsf{T} [M] [\phi] \{\ddot{q}\} + [\phi]^\mathsf{T} [K] [\phi] \{q\} = [\phi]^\mathsf{T} [F] \tag{2.4}$$

$$[I] \{\ddot{q}\} + [\Lambda] \{q\} = \{Q\}, \tag{2.5}$$

where $[\phi]$ is normalized to the mass matrix. This means that the first term in Eq. (2.4) yields the identity matrix $[\phi]^\mathsf{T} [M] [\phi] = [I]$.$[\Lambda]$ is the diagonal matrix containing the

squared eigenfrequencies. The solution of each independent ODE is known from the SDoF system.

Due to the modal transformation the system of linear equations is reduced to N equations. N is the number of eigenvectors, which are used in the transformation for the matrix $[\phi]$. After the transformation each equation represents a decoupled SDoF oscillator.

It is rather difficult to obtain the mass and stiffness matrix experimentally, but it is possible to identify the mode shapes and eigenfrequencies in an experiment, which are mathematically equivalent to the eigenvectors and eigenfrequencies. Equation (2.4) is the *Modal Representation* and equivalent to Eq. (2.3). In practice, however, it is not possible to identify all mode shapes and eigenfrequencies, so Eq. (2.4) is an approximation of Eq. (2.3). It is only possible to obtain the modal parameters of the system in the measured frequency bandwidth. As described in this section, it is possible to transform the physical vector $\{x\}$ into modal coordinates $\{q\}$, also called modal space. If only one eigenvector is considered in Eq. (2.4) then the isolated contribution of this certain mode shape to the dynamic response of the structure is observed. [9]

2.1.4. Modal Approximation of the Dynamic Response

Starting from Eq. (2.2) it is also possible to derive the transfer functions or the so-called frequency response functions (FRF). These functions describe the behaviour of the system due to a harmonic force excitation, e.g. point force or acoustic pressure. It is the ratio between the dynamic response and the applied force of the system. The transfer function can be stated as

$$[H(\Omega)] = \{X\}\{F\}^{-1} = \left(-\Omega^2[M] + j\Omega[D] + [K]\right)^{-1}. \tag{2.6}$$

The solution of Eq. (2.6) is called the direct solution. However, it is also possible to describe the FRF-matrix as set of broken rational polynomial functions:

$$[H(\Omega)] = \sum_i^N \frac{\{\varphi\}_i \{\varphi\}_i^\mathsf{T}}{\left(\Omega^2 - \omega_i^2\right) - 2jD_i\omega_i\Omega}. \tag{2.7}$$

The system is transformed to a set of SDoF oscillators. These polynomial functions are based on the modal damping, mode shapes and eigenfrequencies. If the sum equals the number of DoF, it is an exact representation. The different mode shapes are summed up. The number of DoF can be reduced, if specific mode shapes are omitted. The decoupling

of Eq. (2.1) does not work with every damping matrix. [9]

2.2. Damping Models

A large amount of research has been conducted, in order to achieve a physical damping model to find a proper damping matrix for the finite element analysis. Even nowadays there is no widely used general applicable damping model. State-of-the-art models are non-physical, which allow a simpler mathematical treatment. Often the damping is modelled after a first prototype is built. After the testing, the modal damping values are extracted and applied to the numerical model. Without the structure, it is difficult to estimate the damping. It depends on the experience of the engineer. Some common damping models are presented in this section.

Viscous Damper: This model is used if there is a real damper, like in a car suspension. The viscous damper represents a dashpot damper, so the viscous forces are proportional to the velocity. This will lead to complex mode shapes, because the set of ODEs cannot be decoupled in modal space with this damping model. [2]

Modal Damping: A common method is the so-called modal damping. In Eq. (2.7) the damping ratio D_i for each mode is defined. This means that a viscous damper is added to each decoupled SDoF system in modal space. After performing modal tests on the real structure, the damping ratios are identified and are added to the equation to obtain a more accurate response. [10]

Rayleigh Damping: A more analytical approach is the Rayleigh Damping. The parameters α and β are introduced to calculate the damping matrix according to

$$[D]_{Rayleigh} = \alpha\,[M] + \beta\,[K]\,. \tag{2.8}$$

The damping is calculated using the mass and stiffness matrix. As shown in Sec. 2.1.3, both matrices can be diagonalised with the eigenvectors. So a decoupling of the system of the linear-equations is possible if the Rayleigh damping matrix is transformed into the modal space.

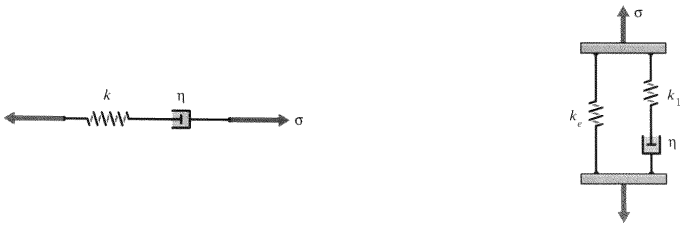

(a) (b)

Figure 2.2.: **Viscoelastic models: (a) Maxwell and (b) Maxwell SLS [14]**

The two parameters are chosen either from experience or from experimental data. With two damping ratios and the corresponding eigenfrequencies, the two parameters α and β can be calculated. The damping ratios at these two chosen eigenfrequencies are exact, whereas the frequency range outside the chosen damping ratios are overdamped. [2, 10]

Structural Damping: Experiments have shown that the material damping depends on the displacement. So the damping matrix depends on the stiffness matrix only and can be calculated according to

$$[D]_{structural} = jg\,[K]\,. \tag{2.9}$$

Also, this damping can be transformed to the modal space easily. This approach is only applicable in frequency domain. This representation violates causality in time domain. Future events affect the current state in time domain. [2]

Viscoelastic Material: Another physical approach is the viscoelastic material modelling. The material is assumed to be viscoelastic, which is true for most polymers. Typical viscoelastic material behaviour is creep and relaxation. If a constant force is applied to a polymer, it will continue to deform with time until a certain value. For a constant displacement, the stress within the polymer will decrease with time. The first phenomenon is called creeping, the latter relaxation, respectively.

Several models have been developed to reproduce the behaviour of viscoelastic material. The most common one is the *Maxwell* and the *Kelvin Voigt* model. These models use springs and dashpots to reproduce the viscoelastic material behaviour. Figure 2.2 (a) shows the Maxwell element. This is a dashpot and a spring in series connection. The Standard Linear Solid (SLS) Maxwell (Fig. 2.2 (b)) simply adds a spring in parallel

connection. The material behaviour of the spring is governed by

$$\sigma = k\varepsilon, \tag{2.10}$$

and the material behaviour of the dashpot is governed by

$$\sigma = d\dot{\varepsilon}, \tag{2.11}$$

where σ is the stress and ε the strain. d and k are material parameters.

The equation governing viscoelastic material behaviour is derived with the known kinematics and Eq. (2.10) and (2.11):

$$\sigma = \left(\left(\frac{1}{j\omega\eta} + \frac{1}{E} \right)^{-1} + E_1 \right) \varepsilon, \tag{2.12}$$

where $j\omega$ is the complex frequency, η and E are material parameters. Equation (2.12) shows the behaviour of the standard linear solid Maxwell. The complex modulus is frequency dependent. [14]

In this case the modal analysis is no longer valid. The equation of motion cannot be transformed into an eigenvalue problem anymore, therefore it is not possible to decouple the equation of motion with the mode shapes. Equation (2.7) is not valid anymore.

An overview of selected damping models is given. Structural damping is often used in aeroelasticity. Viscoelastic material represents a more proper model, since parts in aircraft are often connected with viscoelastic material. These two models are applied in the simulations presented in Ch. 3. Modal damping is used to benchmark the capability of the proposed method in Ch. 4.

2.3. Damping Identification Methods

Many procedures are available to identify damping. Furthermore, the damping can be identified in time domain or in frequency domain. Damping is also present in different fields, like acoustics or structural dynamics. Some methods try to determine the damping ratio, whereas other methods try to identify the damping matrix directly.

EMA is used to identify eigenfrequencies, mode shapes and damping ratios according to

Sec. 2.1.3. Common methods are for instance Polymax and LSCF in frequency domain or LSCE and ITD in time domain. SSI can be formulated in time or frequency domain. EMA is applicable to data in low frequency range when the modal density is low [16]. However, these methods give a global damping estimation but no information about the local distribution.

Damping can also be identified as a damping matrix. Pilkey et al. [13] presents a summary of methods to identify the damping matrix for FE models. The damping matrix can be derived from FRFs or from measured mode shapes, eigenfrequencies and damping ratios. The damping matrix gives information about the local distribution.

Norambuena et al. [12] proposed a method, which is a time-frequency domain hybrid. It is called Method for Local Damping Identification. The damping ratio is identified from a free vibration response in time domain. Several possibilities are available to obtain free vibration response. Norambuena et al. proposed to apply the inverse Fourier transform to a FRF to compute the impulse response functions. The impulse response function is the free vibration response to an unit impulse function [11]. The impulse responses are segmented into many successive short time blocks, each time block is used to calculate a Fourier Transform. Rearranging the spectra of each Fourier Transform yields a spectrogram, shown in Fig. 2.3 (c). This procedure is called Short Time Fourier Transform (STFT). With a STFT an approximation of the decay rate of the magnitudes at each frequency bin is possible. In order to approximate the decay rate, curve fitting is applied, as shown in Fig. 2.4. The whole process is depicted in Fig. 2.5.

Input Data: The presented algorithm identifies the damping from free vibration responses. The FRFs are usually measured in tests and available for future analysis. The inverse Fourier transform of those FRF are the impulse response function, which is a special case of a free decay curve [11]. The transform from frequency to time domain is shown in Fig. 2.3 (a) and (b).

Spectrogram: The Fourier transform represents time data in frequency domain as a spectrum. If frequency or amplitude of the vibration changes over time, this information will be lost after transforming into frequency domain.

In order to overcome this drawback a spectrogram is calculated, which shows the frequency data after a specific time step, so changes in time can be determined. It can be seen as a moving window through the time signal, from which the Fourier transform is calculated after each time step. The length of the window is the measurement time

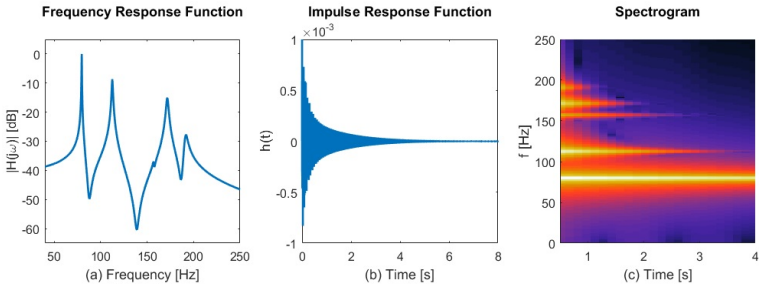

Figure 2.3.: **Example of the first three processing steps described in Fig. 2.5. [12]**

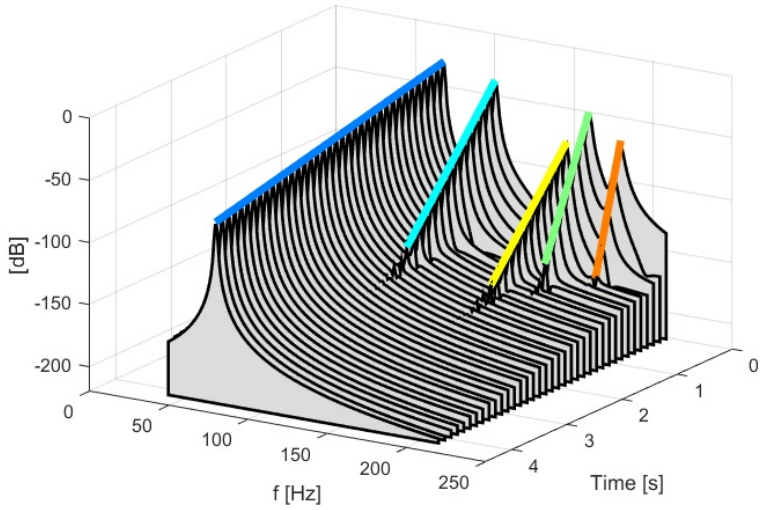

Figure 2.4.: **Spectral decay of the impulse response function together with the fitted decay lines for each of the five resonance peaks. [12]**

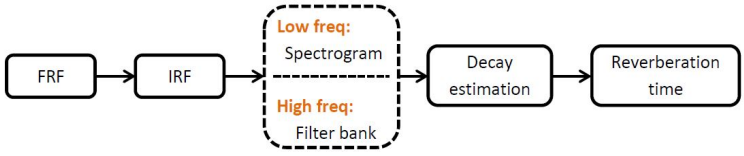

Figure 2.5.: **Schematic of the processing chain to estimate the reverberation time for low and high frequency. [12]**

of each Fourier transform. The relations from the Fourier transform are still valid. The frequency resolution depends on the measured time:

$$\Delta f = \frac{1}{T_{\text{step}}}, \tag{2.13}$$

where Δf is the frequency resolution and T_{step} is the time step between each Fourier transform. Equation (2.13) shows that it is a trade off between time and frequency resolution. It is not possible to have a high time resolution and a high frequency resolution at once. A high time resolution in the spectrum requires short samples for adjacent Fourier Transforms. This will lead to low frequency resolution. Whereas, long measurement time is necessary for a good frequency resolution.

Typically, an overlap between two time windows is used to reduce information loss and increase time resolution in the spectrum. Figure 2.3 (c) shows a spectrogram of a 5 DoF vibration. Each mode is decaying in its frequency.

Other methods to calculate a spectrogram are described in the literature [11]. Another way of analysing the frequency bins individually is the use of filter bank. In this case, each frequency of interest is filtered from the original signal. These filtered signals can be processed independently. Filter bank is common in the field of acoustics.

Decay Estimation: The decay is approximated in each frequency bin of the spectrum. For this purpose a method from room acoustic is used. The Schroeder integral is calculated, from which it is possible to obtain the reverberation time. The Schroeder Integral of an decaying sine signal is shown in Fig. 2.6. The oscillating time signal is transformed into a linear decay. In order to achieve this the y-axis is shown in logarithmic scale. Usually the time needed for the signal to drop to $-60\,\text{dB}$ is measured. However, this is difficult to measure because the signal will vanish in the presence of background noise in a real measurement. So the drop for $-20\,\text{dB}$ is measured and the time is extrapolated. In the field of acoustics, the starting time begins at $-5\,\text{dB}$ in order to avoid the influence of the direct sound or strong early reflections [6]. The measured range is marked with dotted lines in Fig. 2.6 (b). The measurement can also be reduced to a $10\,\text{dB}$ or increased to a $30\,\text{dB}$ drop. The reverberation time is extrapolated accordingly. The damping ratio is then calculated according to [12]:

$$D \approx \frac{1.1}{T_{60} f}. \tag{2.14}$$

Figure 2.4 shows the decay of different modes in one spectrum. This is done for each frequency bin and each measurement point which results in a spatial damping

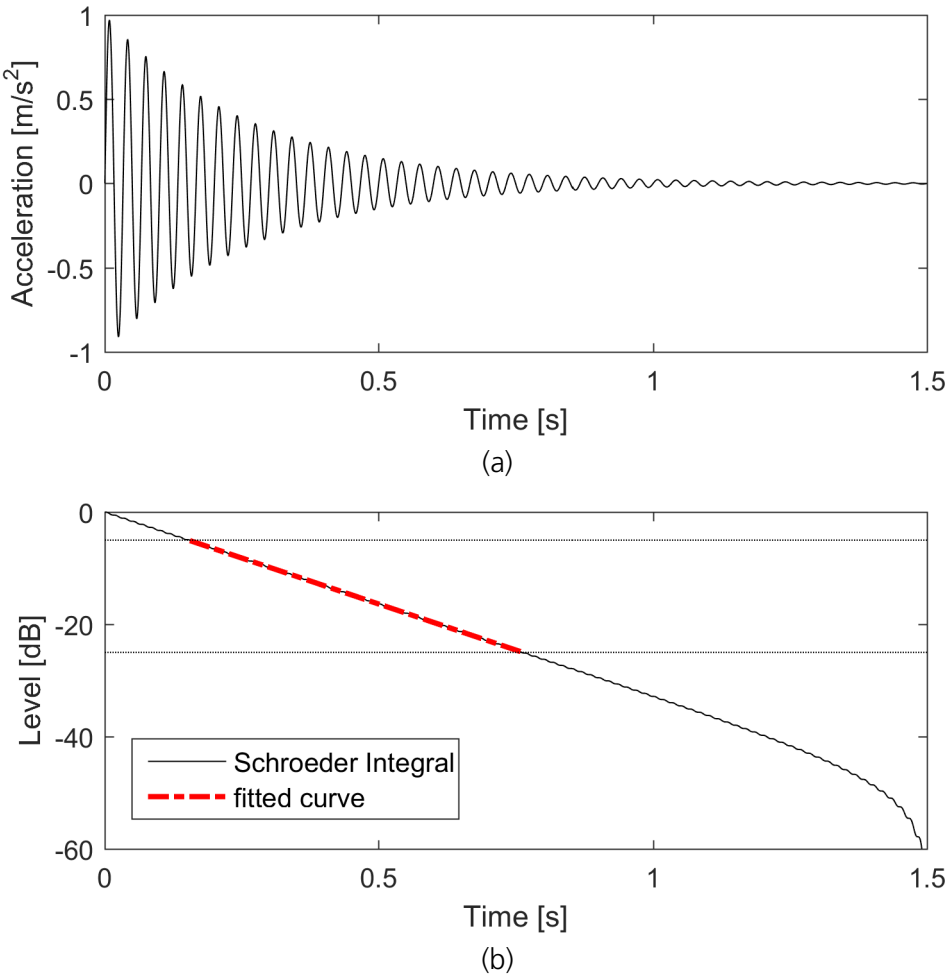

Figure 2.6.: **Example Schroeder Integral of a decaying sine. (a) free vibration decay and (b) Schroeder Integral**

distribution.

In the following chapters the Method for Local Damping Identification is used. Norambuena et al. [12] used the method on experimental data of an aircraft fuselage to identify the damping ratio in the low frequency range in order to compare it with the results from EMA. A damping distribution of the fuselage was calculated. This thesis presents a review of the aforementioned method in order to validate and test the results concerning the estimation of damping distributions.

3. Local Damping Identification for the Low-Frequency Range

In this chapter the verification of the Local Damping Identification Method is conducted. It is tested if applied damping distributions to a FE Model are identified by the Local Damping Identification Method. The structure of interest is an airplane fuselage. A fuselage typically consists of three main components: a cylindrical skin, stringers and frames. Figure 3.1 illustrates a schematic drawing of a fuselage. The sheet metal wrapping around the fuselage is called skin, the supporting structure in longitudinal direction is called stringer and the supporting structure in circumferential direction is called frame. The skin enclosed by stringers and frames is called skin field. Between the skin and stringer is a thin layer of sealing. The stringer or frame and skin are mounted with a high initial tension, so no relative movement between those parts should occur. It is assumed that this thin layer has viscoelastic material behaviour.

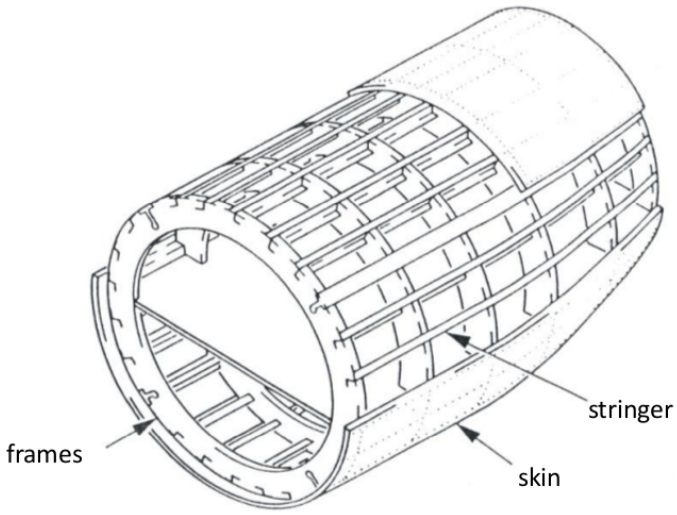

Figure 3.1.: **Schematic drawing of a fuselage [8]**

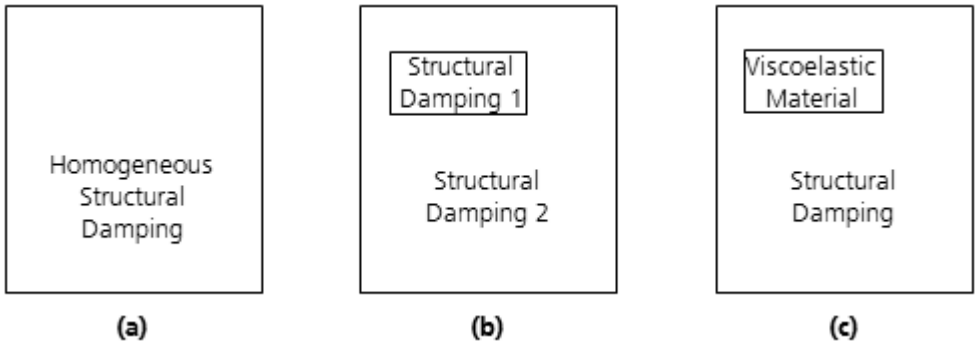

Figure 3.2.: **The three test cases. (a) homogeneous damping distribution, (b) inhomogeneous damping distribution and (c) plate with a viscoelastic patch**

Damping mechanisms within a fuselage can be friction between stringer, frames and skin and internal material damping. Also, radiation loss damping is possible [7]. The air damps the structure with its inertia and internal friction.

Norambuena et al. [12] calculated damping distributions in the low-frequency range, so the damping distribution is analysed in the low-frequency range. This chapter reviews the applicability of the Local Damping Identification.

In order to verify the Local Damping Identification Method the skin field is simplified as a rectangular flat plate without any stringer or frame. Three test cases with increasing complexity are considered as shown in Fig. 3.2. The simplest case has a homogeneous structural damping distribution, see Fig. 3.2 (a). In the second case, a patch with an increased structural damping is applied to the plate, Fig. 3.2 (b). The last case is the most realistic one since it includes a viscoelastic material behaviour which is present in the connection between stringer and skin in a fuselage of an aircraft, Fig. 3.2 (c). The first case is chosen in order to prove if the method is capable to calculate homogeneous damping distributions. Secondly, it is of interest whether the method is able to detect areas of increased damping within a structure. The accurate prediction of a more complex damping behaviour is verified in the third case.

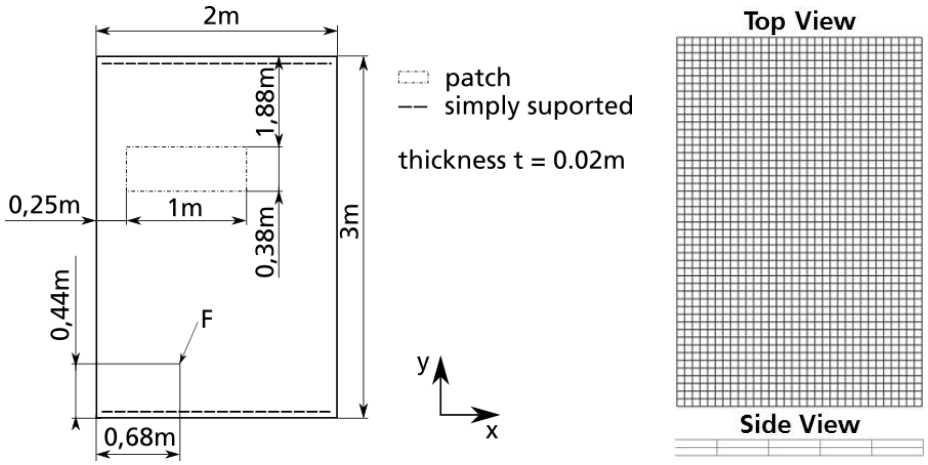

Figure 3.3.: **Analytical Model. (a) Dimensions of the plate and (b) FE Model**

3.1. Simulation Model

As already mentioned, the skin field of a fuselage is simplified as a rectangular plate. The material of the plate is set to aluminium. The dimensions of the plate are 2 m by 3 m with a thickness of 0.02 m. The top and the bottom of the plate is fully supported in order to avoid rigid body modes. The dimensions are chosen arbitrarily. Figure 3.3 (a) depicts the dimensions of the analytical model. The force F is applied normal to the plate surface at the bottom left corner, as shown in Fig. 3.3 (a). This force has a constant amplitude of 1 N for all analysed frequencies. In the marked patch in Fig. 3.3 (a) different material properties are modelled to examine different damping effects. The patch has a horizontal and vertical offset from the midpoint. This placement is chosen to avoid symmetry.

FE Model: The rectangular plate is discretised with linear hexahedral elements, also known as brick elements. The mesh of the FE Model is shown in Fig. 3.3 (b). It has 32 elements in x-direction and 48 elements in y-direction. 2 elements are placed along the height. The mesh consists in total of 4851 evenly distributed nodes. Each element has an edge length of 0.0625 m in width and height and a thickness of 0.01 m. A full 3D model is chosen, so stringers can be added consistently as a 3D model as well. In a convergence study modal parameters are computed through modal analysis. The number of nodes is doubled in every computation and an eigenfrequency above 500 Hz

is monitored. For the aforementioned number of elements the monitored frequency converged. This is a fine mesh which is also accurate in the higher frequencies. Also the spatial resolution of available data is high, since every node is one measurement point.

The used material parameters for the FE Model are listed in Table 3.1. The Young's Modulus E is set to $7 \times 10^{10}\,\mathrm{N\,m^{-2}}$, the density ρ to $2700\,\mathrm{kg\,m^{-3}}$ and the Poisson ratio ν to 0.34. This material behaviour is chosen to those of aluminium. A structural damping coefficient g of 5 % is applied to the plate which yields a critical damping ratio of 2.5 %. The maximum calculated damping ratios presented by Norambuena et al. [12] are between 2 % and 3 %, so the average of 2.5 % is chosen. In the first two cases the material properties of the patch are also set to aluminiums. The structural damping coefficient of the patch is also 5 % in the first case in order to have a homogeneous damping distribution. In the second case the structural damping coefficient of the plate is increased to 10 %. In the third case the patch material properties is chosen to those of polymers and the overall structural damping coefficient for the whole plate is set to 0.5 %.

Mode Shapes A numerical modal analysis of the undamped structure is performed to compute the eigenfrequencies and the real mode shapes. Figure 3.4 shows mode 2 at 11.6 Hz, mode 3 at 21.3 Hz, mode 7 at 56.5 Hz and mode 8 at 57.4 Hz. These mode shapes are picked arbitrarily, for the sake of illustration. The shown mode shapes are normalised, so that the maximum displacement is one. Mode 2 in Fig. 3.4 (a) has a vertical nodal line in the middle at 1 m in x-direction. Horizontally it looks like a half cosine and vertically like a half sine. Mode 3 in Fig. 3.4 (b) has a horizontal nodal line in the middle at 1.5 m in y-direction. The deformation horizontally is constant, whereas the vertical displacement behaves like a sine wave. Mode 7 in Fig. 3.4 (c) shows 3 nodal lines: One horizontally in the middle at 1.5 m in y-direction and two vertically approximately one fourth from each side at 0.25 m and 1.75 m in x-direction. The shape looks like a full cosine wave horizontally and a full sine wave vertically. The 8th mode

Table 3.1.: **Material parameters for homogenous plate**

	E [$\mathrm{N\,m^{-2}}$]	ν [-]	ρ [$\mathrm{kg\,m^{-3}}$]	g[%]
plate	7e10	0.34	2700	5
patch 1	7e10	0.34	2700	5
patch 2	7e10	0.34	2700	10
patch 3	1e6	0.4	1000	viscoelastic

in Fig. 3.4 (d) also has 3 nodal lines. This mode shape has one nodal line vertically at 1 m in x-direction and two horizontally at 1 m and 2 m in y-direction. The horizontal displacement is like a half cosine and the vertical displacement is like one and a half sine.

Output: The FRF of the plate shown is computed as input for the method described in Sec. 2.3. The FRF is calculated from 0 Hz to 2000 Hz with a frequency step of 0.25 Hz. The discrete acceleration responses of the plate are used as output. Although the FRF is not analysed up to 2000 Hz, it is necessary to compute up to this high frequency to provide a high time resolution with the inverse Fourier transform. The relation between time resolution Δt and the maximum analysed frequency f_{max} in frequency domain is

$$\Delta t = \frac{1}{2 f_{max}}. \tag{3.1}$$

The direct solution according to Eq. (2.6) is chosen in order to calculate the FRFs of the plate. Thus, the FRFs are computed directly in physical space and is not approximated by a limited number of modes. The analysis in the following sections calculates the local damping distribution in the low-frequency range up to 100 Hz. As already mentioned, the frequency response function is assumed to be correct up to 500 Hz. Noise is neglected in the simulations.

3.2. Application of the Local Damping Identification Method with Homogeneous Structural Damping

This section examines the damping distribution of the plate calculated by the Local Damping Identification Method. The applied damping distribution in the simulation model is homogeneous. First the model with all modes is considered, called the Full Model, then the model is reduced to single modes, in order to investigate the behaviour of isolated modes. The FRF of the reduced models are computed in modal space and not with the direct solution.

The damping distribution is calculated according to the method described in Sec. 2.3. For the STFT a Hanning window with 200 ms length and a 50 % overlap is chosen. This yields a frequency band of 5 Hz. These are the same parameters as used by Norambuena

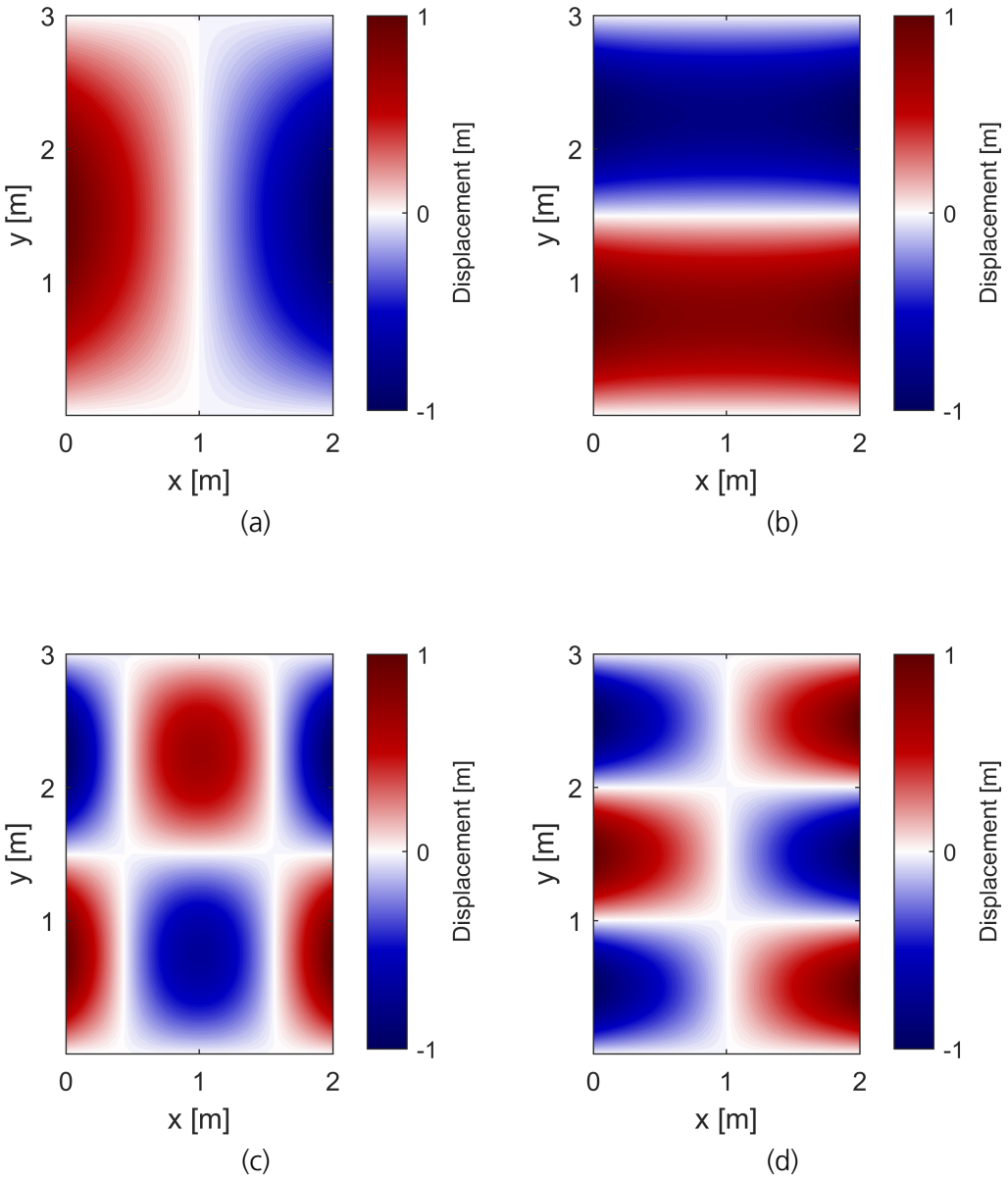

Figure 3.4.: **Computed Mode Shapes. (a) Mode 2 at** 11.6 Hz**, (b) Mode 3 at** 21.3 Hz**, (c) Mode 7 at** 56.5 Hz **and (d) Mode 8 at** 57.4 Hz

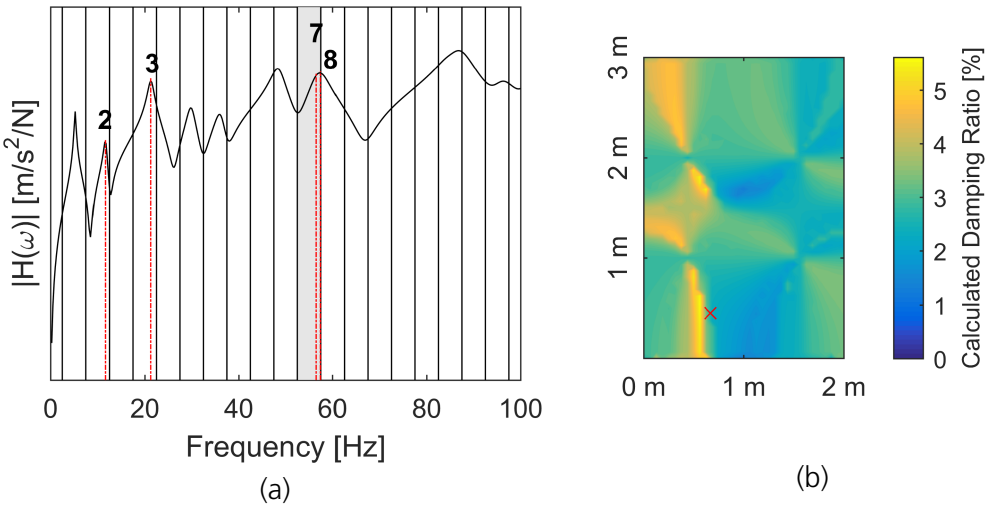

Figure 3.5.: **(a) Frequency Response Function at driving point and (b) Damping Map** $\overline{D} = 3.0\,\%$ **at** $55\,\mathrm{Hz}$

et al. [12]. The analysed frequency bands are narrow compared with the ones usually used in acoustics. The vertical lines in Fig. 3.5 (a) show the frequency bands. It can be seen that approximately one mode per band is present. The grey band shows the analysed band for the damping distribution in Fig. 3.5 (b). The time until a $-30\,\mathrm{dB}$ drop of the signal is used to calculate the damping ratios.

Full Model: The FRF at the driving point is shown in Fig. 3.5 (a). The driving point is the point where the applied force is located, marked with a red cross in Fig. 3.5 (b). The mode shapes from Fig. 3.4 are marked according to their number in this plot.

The results in the bands outside of the eigenfrequencies do not yield physically reasonable results, since no vibration at these frequencies occurs. Figure 3.5 (b) shows the calculated damping distribution for $55\,\mathrm{Hz}$ with a bandwidth of $5\,\mathrm{Hz}$. It can be observed in the FRF and also from the modal analysis that two eigenfrequencies are present in this band. Although a homogeneous damping distribution is applied to the FE Model, it is obvious that the results of this method are not reflecting the applied damping distribution. The mean value however is close to the applied damping ratio.

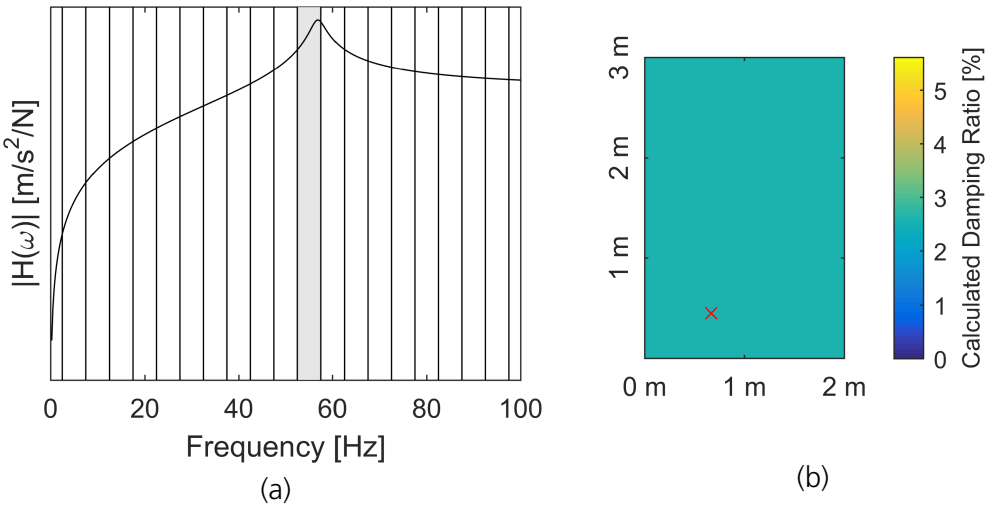

Figure 3.6.: **(a) Frequency Response Function at driving point reduced to mode 7 and (b) Damping Map $\overline{D} = 2.6\,\%$ at** $55\,\mathrm{Hz}$

Modal Reduction to Mode 7: In order to understand the behaviour of the damping identification algorithm the numerical model is simplified. According to Sec. 2.1.3 the plate is reduced to a SDoF vibration, approximating the dynamic response of the plate with the contribution of a single mode according to Eq. (2.7). Only the contribution of mode 7 to the dynamic response of the plate is considered in this calculation and the damping distribution based on this single mode is calculated. The FRF and the damping distribution of this system is illustrated in Fig. 3.6. The calculated damping distribution in Fig. 3.6 (b) is at 55 Hz. This is the highlighted band in Fig. 3.6 (a).

In this case the identified damping ratio is equally distributed as expected. But instead of the theoretical value of $2.5\,\%$ the damping ratio is slightly overestimated at $2.6\,\%$. Equation (2.14) shows that the damping ratio depends on the analysed frequency. This method uses the centre-frequency of the analysed frequency band f_{center} to calculate the damping ratio. If the centre-frequency is lower than the eigenfrequency, the damping ratio will be higher. The centre-frequency used for this calculation is slightly lower than the eigenfrequency of mode 7. So the damping ratio is slightly overestimated. Since the actual frequency of vibration is known, it can be corrected according to

$$D_{\mathrm{real}} = D_{\mathrm{calc}} \frac{f_{\mathrm{center}}}{f_{\mathrm{real}}}. \tag{3.2}$$

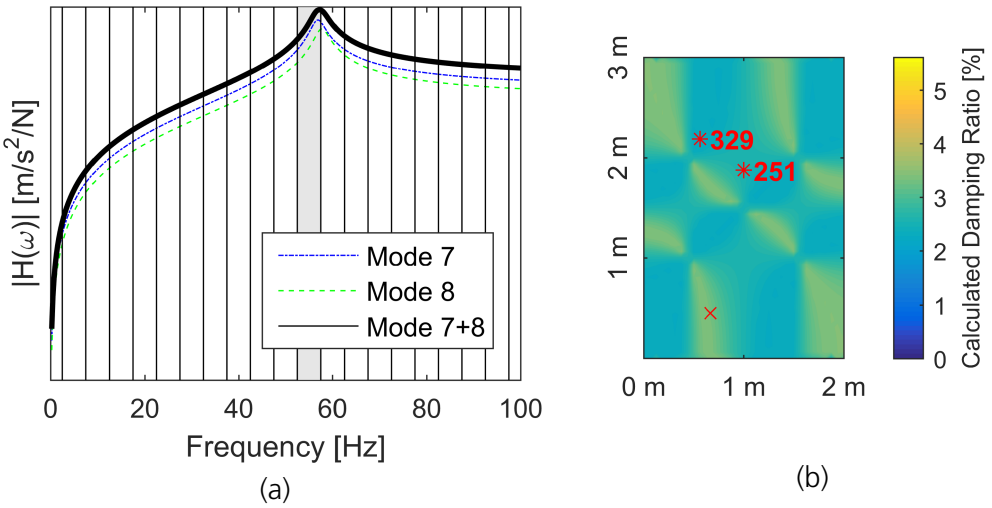

Figure 3.7.: **(a) Frequency Response Function at driving point reduced to mode 7 and 8 and (b) Damping Map $\overline{D} = 2.7\,\%$ at** $55\,\mathrm{Hz}$

Modal Reduction to Mode 7 and 8: The calculated damping distribution in Fig. 3.5 (b) shows a pattern, whereas Fig. 3.6 (b) shows a homogeneous distribution. In order to investigate the reason for this pattern in the calculated damping distribution, an additional mode is considered in the dynamic response approximation. Figure 3.7 (a) shows the FRF at the driving point of the plate reduced to mode 7 and 8. The FRF still looks like a SDoF vibration because the included modes are very close in frequency. Both contributions of the modes add up to a stronger response in this frequency range. The damping distribution illustrated in Fig. 3.7 (b) shows a pattern which is similar to the mode shapes of mode 7 and 8 in Fig. 3.4.

The inverse Fourier transform of the simulated FRFs is calculated, in order to analyse the time domain data. The reason for the illustrated pattern in Fig. 3.7 (b) is found in this data. Node 329 and 251 of the FE model are marked in Fig. 3.7 (b). For each node a FRF is available, so it is comparable to measurement points. For those two nodes, the impulse response in time domain is shown in Fig. 3.8 (a) and (c) respectively. In Fig. 3.8 (c) the envelope of the decaying sine is increasing and then decreasing. This behaviour is the so-called beat phenomenon.

The beat phenomenon is present when two modes with close frequencies interact. The envelope of the two sines forms a wave with the frequency half the difference of the two original sines. It depends on the phase shift between the two sines whether the envelope increases or decreases first. Figure 3.9 shows the phenomenon of beat with

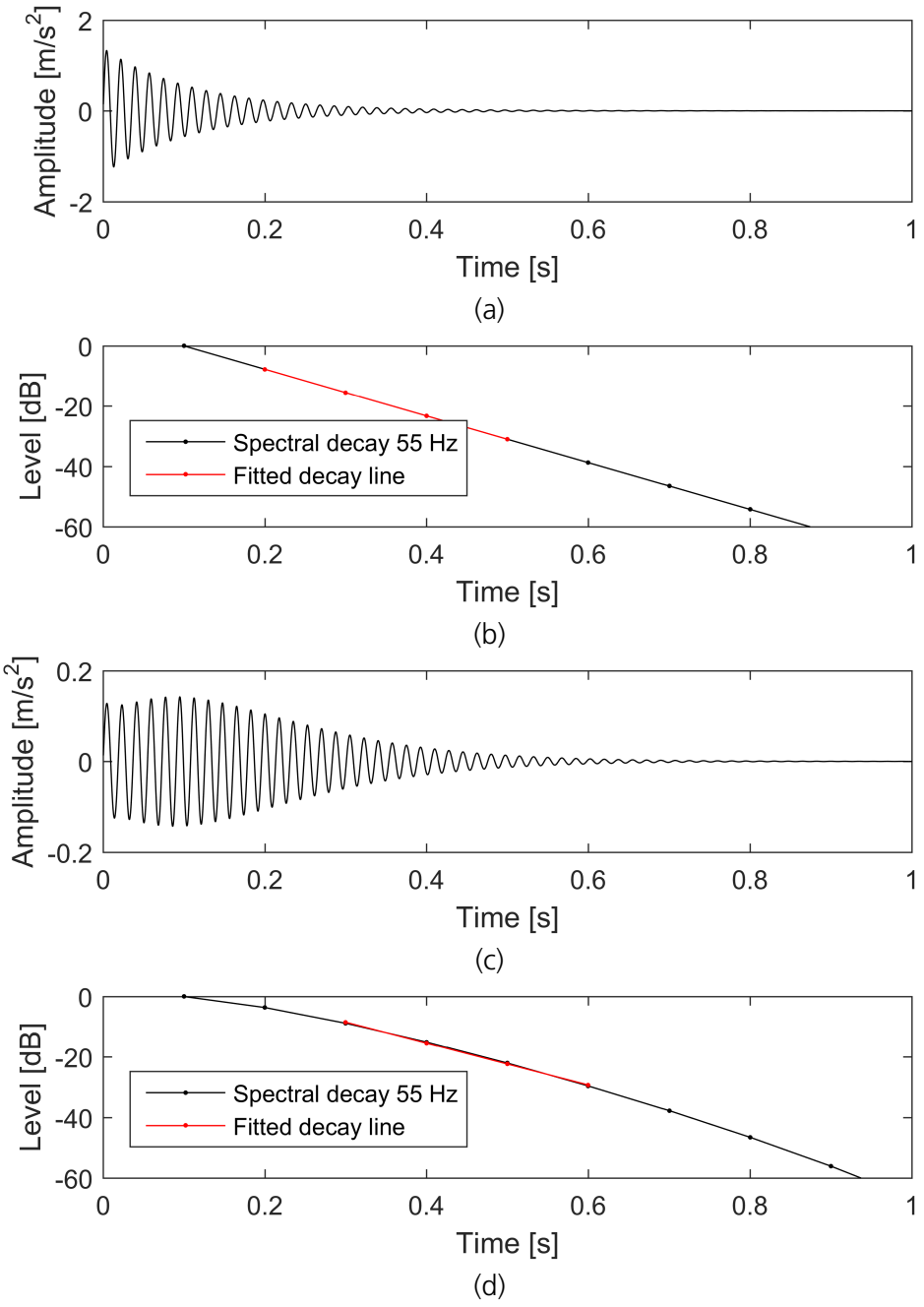

Figure 3.8.: **Decay in time domain (mode 7 & 8). (a) Impulse Response Node 251, (b) Schroeder Integral Node 251 with $D = 2.58\,\%$, (c) Impulse Response Node 329 and (d) Schroeder Integral Node 329 with $D = 2.31\,\%$**

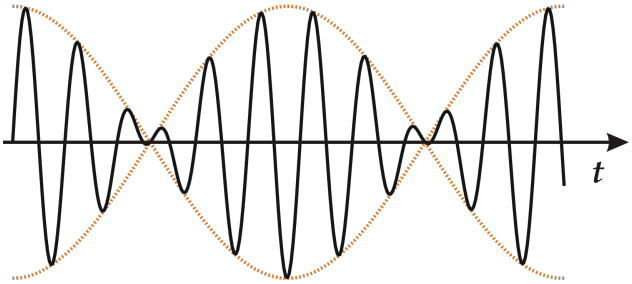

Figure 3.9.: **Diagram of beat frequency [15]**

two sine functions. [9]

The calculated damping ratio will be underestimated if the envelope of the impulse response is increasing first. The Schroeder integral of the impulse response of Node 329 is shown in Fig. 3.8 (d). The slope of the curve is increasing with time due to the beat effect.

Modal Reduction to Mode 2 and 3: It has been shown that two modes in a frequency band lead to a calculated damping distribution of the plate which is not physically driven. In order to investigate if a mode outside the regarded frequency band influences the calculated damping distribution, the system is simplified again. In the following analysis only mode 2 and 3 are considered to contribute to the dynamic response of the plate.

A drop of 20 dB is used in order to calculate the damping ratios. Figure 3.10 (a) shows the FRF and Fig. 3.10 (b) depicts the calculated damping distribution of mode 2 and 3. The analysed frequency band from 18.5 Hz to 22.5 Hz is marked grey. In that frequency band, only one mode shape is present. Also the modal analysis states that only one mode exists between 18.5 Hz and 22.5 Hz. The first mode is around 12 Hz, meaning that there is one frequency band between those two modes. Analysing these two modes separately, the calculated damping distribution is homogeneous as illustrated in Fig. 3.6 (b). The calculated damping distribution of this case, with two modes, illustrated in Fig. 3.10 (b) shows a non-homogeneous distribution. The damping is homogeneous except for the horizontal centre line. Comparing with the mode shape in Fig. 3.4 this line is a nodal line of mode 3 in the analysed frequency band.

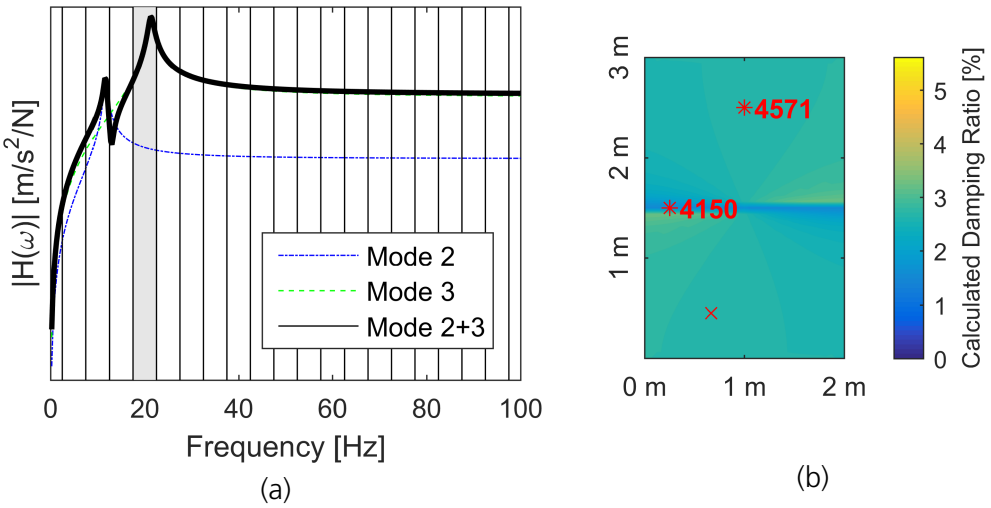

Figure 3.10.: **Frequency Response Function at driving point reduced to mode 2 and 3. (a) Frequency Response Function and (b) Damping Map** $\overline{D} =$ 2.64 % **at** 20 Hz

The time domain data is examined again. Figure 3.11 (a) and (c) show the time domain data of the marked nodes in Fig. 3.10 (b). Node 4150 is on the nodal line of mode 3 so only mode 2 is responding and Node 4571 is on the nodal line of mode 2 so only mode 3 is responding. Because the nodes are on the nodal line of each mode shape, these nodes behave like SDoF systems. Figure 3.11 (a) shows the decay of the impulse response of the second mode and (c) shows the decay of the third mode. The Schroeder integral of both signals is shown in Fig. 3.11 (b) and (d), respectively. The deviation from the theoretical value of 2.5 % can be explained by Eq. (3.2). The nodal line of mode 3 has a lower damping ratio because the response of the second mode only is present. Transferring the damping ratio of the second mode to the frequency of the third mode through Eq. (3.2) will result in a lower damping ratio. The damping ratio of the second mode is slightly overestimated because the eigenfrequency is higher than the analysed centre-frequency. If the calculated damping distribution is analysed at 10 Hz then the nodal line of the second mode has a higher damping ratio.

The modes outside of the analysed band have an influence on the calculated damping distribution. The analysed data are taken directly from a computer simulation. Noise in the signal is neglected. The influence of modes outside the analysed frequency band might be hidden due to the signal noise. Nevertheless, if modes are present in neighbouring frequency bands, then it may affect the damping identification and an accurate estimate of the local damping distribution is not possible.

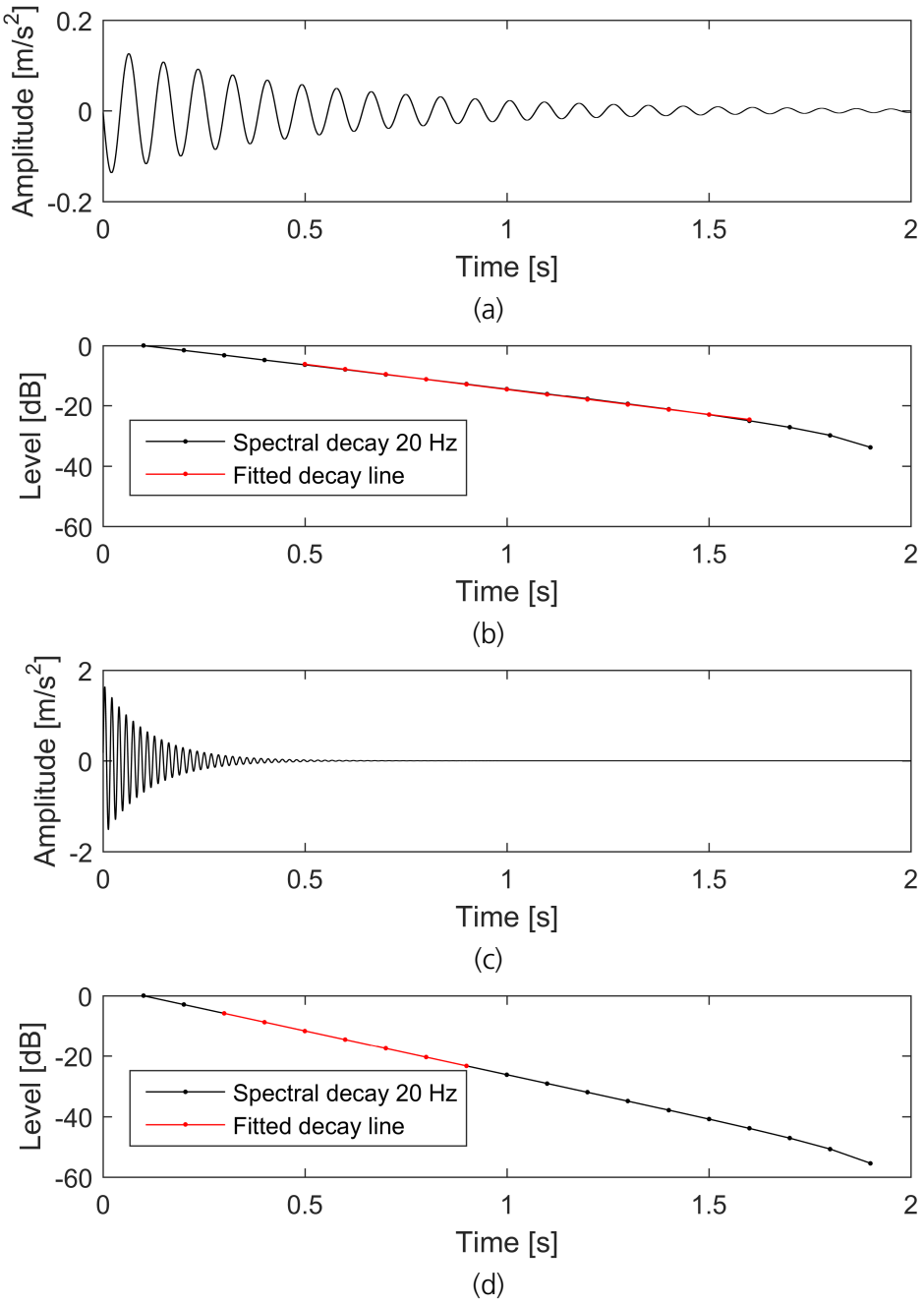

Figure 3.11.: **Decay in time domain (mode 2 & 3). (a) Impulse Response Node 4150, (b) Schroeder Integral Node 4150 with $D = 1.54\,\%$, (c) and Impulse Response Node 4571 and (d) Node 4571 Schroeder Integral with $D = 2.66\,\%$**

3.3. Application of the Local Damping Identification Method with Inhomogeneous Structural Damping

The FE model is still the one depicted in Fig. 3.3. However, the patch within the plate has a higher structural damping coefficient. The parameters are written in Table 3.1. The applied structural damping coefficient within the patch is 10 % and thus twice as high as the applied structural damping coefficient in the rest of the plate at 5 %. The other properties remain the same. The parameters for the Local Damping Identification Method are also the same, i.e. the frequency band is 5 Hz. The damping ratios are approximated with a 30 dB drop.

Figure 3.12 (a) shows the FRF of the plate with the damping patch at the driving point and (b) the corresponding calculated damping distribution. The analysed frequency band is highlighted again in Fig. (a). In order to compare the results with the previous ones, the frequency band around the centre-frequency of 55 Hz is chosen again. The FRF and also the calculated damping distribution is similar to the analysis with a homogeneous plate. The patch with a different applied damping coefficient, highlighted in Fig. 3.12 (b), is not identified in the calculated damping distribution by the method. The calculated damping distribution is similar to the calculated damping distribution of the plate with applied homogeneous damping distribution depicted in Fig. 3.5 (b). The conclusions from Sec. 3.2 are also valid for this case. The damping map shows the interference of different modes inside and outside the analysed frequency band. However, the mean value of the damping ratios increased to 3.1 %. This makes sense, since the applied damping in the patch is increased.

It is not possible to find the applied damping distribution for this model using the current method. The discussed method identifies the damping ratio as a decay in time domain, as shown in Sec. 2.2. Structural damping is proportional to the stiffness matrix, which means that it can be diagonalised in modal space, so the Eq. (2.7) is valid. After decoupling the equation of motion, every mode has a single global damping ratio. This means that the damping is distributed homogeneously over the whole plate. With the given assumption the method for local damping identification is not able to identify homogeneous damping distributions due to the interaction of adjacent modes. However, the interaction in the presented examples is accentuated by the fact that no noise was introduced in the simulations performed.

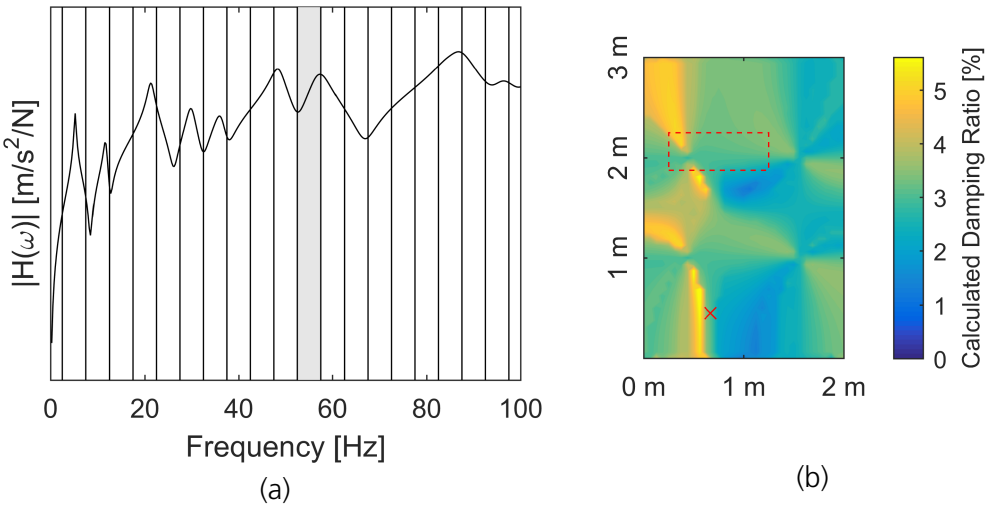

Figure 3.12.: **(a) Frequency Response Function at driving point of the inhomogeneous plate and (b) Damping Map $\overline{D} = 3.1\,\%$ at** $55\,\mathrm{Hz}$

3.4. Application of the Local Damping Identification Method with Viscoelastic Damping

Again the plate depicted in Fig. 3.3 is used. The FRF of the plate with a global structural damping coefficient of $0.5\,\%$ is analysed. The patch has viscoelastic material behaviour as described in Sec. 2.2. Modal analysis is not valid for this material behaviour, since the material model is frequency dependant. The equation of motion (2.1) cannot be decoupled.

The Maxwell SLS element is chosen to model the viscoelastic material behaviour. The complex modulus is described by Eq. (2.12) as a function of frequency for the Maxwell SLS element. The real part is equivalent to Young's Modulus and the imaginary part is the loss modulus. Arbitrary values are applied to reproduce viscoelastic behaviour. The stiffness is chosen according to a polymer. The properties are written in Table 3.1.

Figure 3.13 (a) shows the FRF at the driving point. It can be seen that the eigenfrequencies are shifted to a lower frequency because the patch is less stiff. The calculated damping distribution is shown in Fig. 3.13 (b). Again the analysed frequency band is

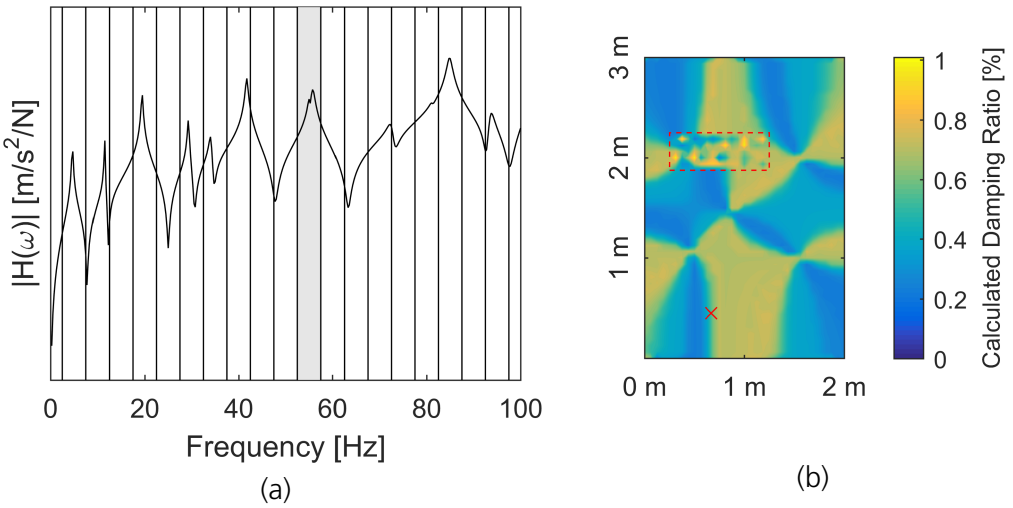

Figure 3.13.: **(a) Frequency Response Function at driving point of the plate with a viscoelastic patch (b) Damping Map $\overline{D} = 0.5\,\%$ at** 55 Hz

from 48.5 Hz to 52.5 Hz. The calculated distribution is similar to the damping maps of the previous plates with the difference that the maximum damping value is smaller. The mean value of the damping ratios is 0.5 %. The patch seems to behave differently, but it is not possible to tell if the damping value is higher or lower.

3.5. Conclusion Local Damping Identification

Considering the specific cases presented here, the simulation models show that the algorithm calculates damping distributions in each frequency band. These calculated distributions are not of physical nature. They are correlated to the mode shapes. Due to the beat effect of neighbouring frequencies, the envelope of the transient response is superimposed by an additional sine curve with a low frequency which lead to a wrongly detected decay.

However, the mean value of the calculated damping ratios of the analysed frequency band is close to the applied damping ratio. The next chapter investigates if these mean values can be applied in a FE model as a global damping ratio to simulate the structural response behaviour.

The curve fits show that the time resolution of the STFT is sometimes not sufficient, since not enough data points are available. The implementation of filter bank can improve the time resolution. An appropriate filter in time domain is presented by Goyder et al. [5]. The filter can also be in frequency domain, as shown in the technical report by Bruel and Kjaer [4]. A high frequency resolution is necessary to achieve proper results.

Other damping models could be tested as well. For friction models, contact needs to be taken into consideration which makes the model much more complex.

4. Global Damping Identification for the Mid-Frequency Range

This chapter discusses the damping identification in the mid-frequency range. EMA is not capable of estimating a proper damping value due to the high modal density and overlap. This means that individual modes are too close to be identified. The proposed damping identification method calculates a damping ratio D_{local} which depends on frequency and location:

$$D_{\text{local}} = D_{\text{local}}(f, \{x\}), \tag{4.1}$$

so a spatial damping distribution is obtained. Whereas EMA provides a global damping ratio, only dependent on the eigenfrequency:

$$D_{\text{EMA}} = D_{\text{EMA}}(f_i). \tag{4.2}$$

Winter et al. [16] showed that the mean value of a calculated damping distribution at one certain frequency is close to the global damping ratio obtained by EMA. The previous chapter showed that the damping distribution with the assumptions taken are not driven by physics. However, the Local Damping Identification Method also calculates damping ratios in the mid- and high-frequency range. In this chapter the global damping ratio is reviewed by spatially averaging the damping ratios obtained at one frequency band f_n:

$$D_{\text{global}}(f_n) = \text{mean}(D_{\text{local}}(f_n, \{x\})). \tag{4.3}$$

The decay time at higher frequencies is lower than the decay time at lower frequencies for an equal damping ratio. Reordering Eq. (2.14) yields:

$$T_{60} \approx \frac{1.1}{Df}. \tag{4.4}$$

For a damping ratio of $D = 2.5\,\%$, the decay time at $f = 10\,\text{Hz}$ is $4.40\,\text{s}$, whereas, the decay time at $f = 100\,\text{Hz}$ is $0.44\,\text{s}$ with the same damping ratio. So the time resolution in the spectrogram needs to be increased. However, good time resolution leads to a lower frequency resolution as described by Eq. (2.13). A time step of $T_{\text{step}} = 200\,\text{ms}$ lead to a frequency resolution of $\Delta f = 5\,\text{Hz}$, while a time step of $T_{\text{step}} = 10\,\text{ms}$ yield a frequency resolution of $\Delta f = 100\,\text{Hz}$. Thus the damping ratio is not assigned to a single frequency, but a frequency range, which can be seen as an equivalent damping ratio to a frequency band. The damping ratio is also averaged in frequency, due to the wider frequency bands. So the damping ratio calculated in this chapter is a global equivalent damping ratio.

Due to the wide frequency band, several modes are present in one frequency band. First the influence of more than one mode in one frequency band on the equivalent damping ratio is investigated in a parameter study. Then, the needed number of measurement points is studied in order to obtain a good approximation of the global damping ratio as a mean value. Finally, the test case from Sec. 3.3 with inhomogeneous structural damping is taken to calculate the global equivalent damping ratio. These calculated damping ratios are taken and applied to the undamped model described in Sec. 3.1. The FRFs computed by both models are compared.

4.1. Parameter Study of the Global Damping Identification Method to an Analytical Test Case

As discussed in Sec. 2.1.3, a specific eigenfrequency and modal damping value can be assigned to each mode. This section deals with the damping identification in the mid-frequency range, which is characterised by a high modal density. Figure 4.1 shows an example FRF with broad frequency bands. Each analysed frequency band is enclosed by two vertical lines. In every frequency band more than one mode is present. A discussion follows about the calculation of an equivalent damping ratio for a frequency band, with more than one mode.

Instead of a damping ratio for a single mode, the calculated damping ratio within the given frequency band can be seen as an equivalent damping ratio for several modes, as already mentioned. A parameter study is performed with an analytical test case, in order to investigate the influence of three modes in one frequency band on the

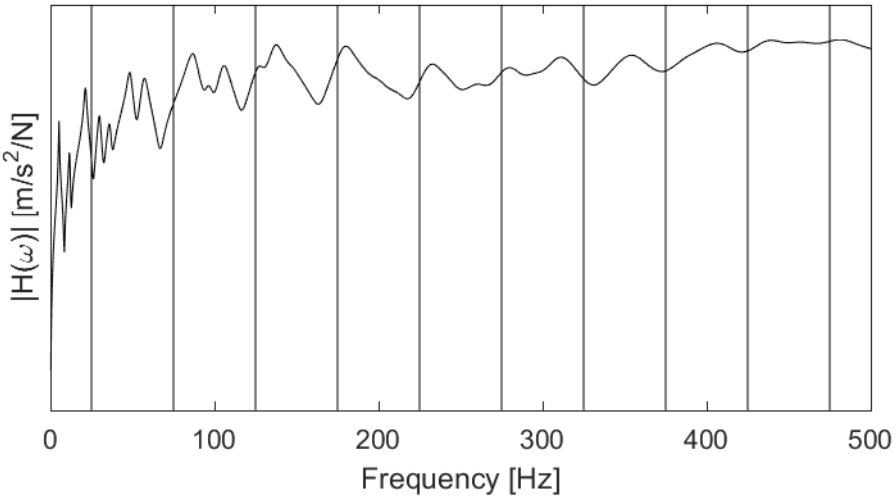

Figure 4.1.: **Example FRF with wide frequency bands**

calculated equivalent damping ratio. The impulse response is approximated with three sine functions with an exponential decay:

$$x = \sum_{i=1}^{N=3} A_i e^{D_i 2\pi f_i t} \sin(2\pi f_i t - \psi_i). \tag{4.5}$$

The frequency f_i, amplitude A_i, the phase shift ψ_i and the damping ratio D_i are defined as parameters. Figure 4.2 shows the test signal x and its components $i = 1$, $i = 2$ and $i = 3$. Each parameter is varied to investigate the sensitivity on the calculated equivalent damping value. In a second analysis the influence of the number of modes, i.e. the number of sine functions, is tested.

The analysis is performed with the centre-frequency at 200 Hz and a frequency band of 100 Hz. This means that the analysed frequencies are from 150 Hz to 250 Hz. One sine is located in the centre-frequency and one above and below the centre-frequency, respectively. The reference parameters are one unit amplitude A_i for all sine functions with no phase shift ψ_i. The individual damping ratio D_i is set to 2.5 % for all considered harmonics. The frequency f_1 is set to 170 Hz, f_2 to 200 Hz and f_3 to 230 Hz as shown in Table 4.1. So $i = 1$ represents a vibration below the analysed centre-frequency, $i = 2$ is a vibration at the centre-frequency and $i = 3$ is a vibration above the centre-frequency.

The calculated equivalent damping ratio with the reference parameters from Table 4.1 is $D_{\text{eq,ref}} = 2.16\,\%$. Figure 4.2 shows the analysed decay curve. The damping ratio

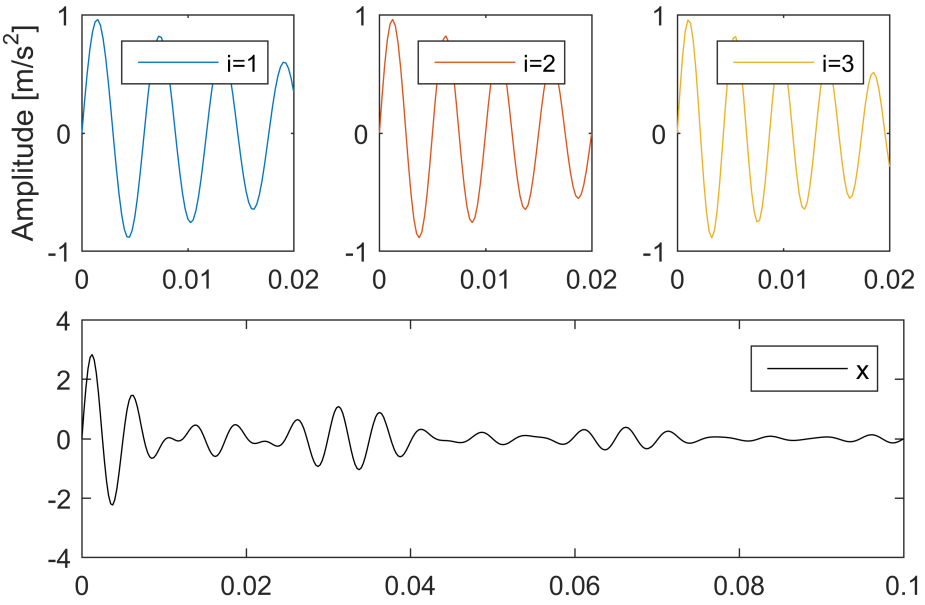

Figure 4.2.: **Composition of the analytical test case**

is underestimated due to the beat effect. All calculated equivalent damping ratios in the parameter study are given as a relative change with respect to $D_{\text{eq,ref}}$. All other parameters are given as a relative change with respect to their corresponding reference parameter in Table 4.1. The variation of the following parameters will be investigated:

- Frequency f_i
- Amplitude A_i
- Damping Ratio D_i
- Phase ψ_i
- Modal Density N

Modal Density is investigated by increasing the number of decaying sine functions N. All other parameters are analysed 3 times from $-20\,\%$ to $20\,\%$ relative change with respect to the reference value shown in Table 4.1. For instance, the three frequencies f_1, f_2 and f_3 for each sine function are analysed separately but will be shown in one plot.

Table 4.1.: **Reference parameters for sensitivity study**

i	$D_{\mathbf{i,ref}}$ **[%]**	$f_{\mathbf{i,ref}}$ **[Hz]**	$A_{\mathbf{i,ref}}$ **[m s^{-1}]**	$\psi_{\mathbf{i,ref}}$ **[°]**
1	2.5	170	1	0
2	2.5	200	1	0
3	2.5	230	1	0

Frequency: Each frequency f_i in Eq. (4.5) is varied from -20% to +20% relative change of the reference value $f_{\mathrm{i,ref}}$. f_1 of the first sine is varied from 136 Hz to 204 Hz, f_2 is varied from 160 Hz to 240 Hz and f_3 is varied from 184 Hz to 276 Hz, respectively. The three frequencies f_i are varied independently, so three variations are done. Figure 4.3 shows the relative change of the calculated equivalent damping ratio $\frac{\Delta D_{\mathrm{eq}}}{D_{\mathrm{eq,ref}}}$ as a function of the relative change of each individual frequency $\frac{\Delta f_i}{f_{\mathrm{i,ref}}}$. Three lines are plotted for each varied frequency f_i. The dashed line of f_1 and f_3 means that the frequency is already outside the analysed frequency band. $f_1 - 11\,\% f_1 = 150$ Hz and $f_3 + 8\,\% f_3 = 250$ Hz.

Three regions can be identified in Fig. 4.3. From $-10\,\%$ to $10\,\%$ relative change of the frequencies, only a small change of the calculated equivalent damping ratio is observed. In the other two regions from $-20\,\%$ to $-10\,\%$ and $10\,\%$ to $20\,\%$ relative change of the frequencies, the relative change of the calculated equivalent damping ratio D_{eq} increases above $50\,\%$.

If the relative change of the frequency is small, the calculated equivalent damping ratio is not affected. If the relative change becomes bigger, the calculated equivalent damping ratio is changing significantly. With increasing relative change, the frequencies are coming closer, so the effect of beating discussed in Sec. 3.2 is increasing. For instance, at $15\,\%$ relative change of f_2, it will take the value $f_2 = 230$ Hz and is the same as the reference value of f_3. So in proximity of $15\,\%$ relative change of f_2 the calculated equivalent damping ratio will increase significantly. The same happens at $-15\,\%$ relative change of f_2. Changing f_1 and f_3 behaves accordingly. If one of the frequencies comes close to another the calculated equivalent damping ratio changes significantly.

Amplitude: Each Amplitude A_i in Eq. (4.5) of the vibrations is varied from 0.8 to 1.2 to study the influences on the calculated equivalent damping ratio. The relative change of the calculated equivalent damping ratio $\frac{\Delta D_{\mathrm{eq}}}{D_{\mathrm{eq,ref}}}$ against the relative change of each individual amplitude $\frac{\Delta A_{\mathrm{i}}}{A_{\mathrm{i,ref}}}$ is plotted in Fig. 4.4.

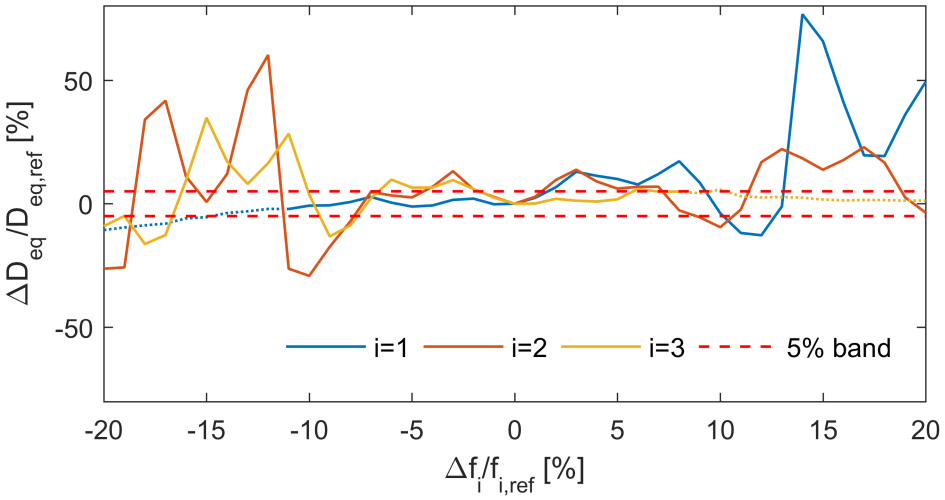

Figure 4.3.: **Variation of the frequencies**

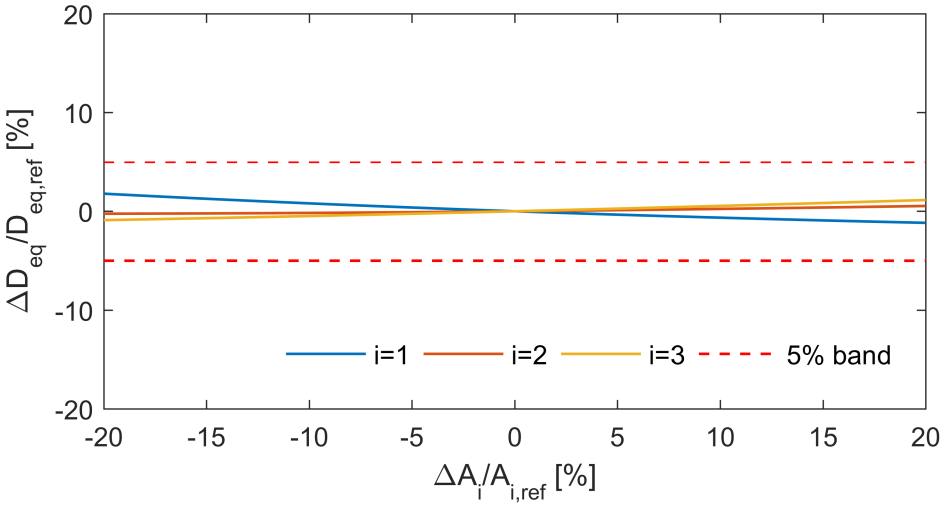

Figure 4.4.: **Variation of the amplitudes**

The blue line shows the variation of the first amplitude A_1. The calculated equivalent damping ratio linearly decreases as the amplitude increases. The maximum relative change of the calculated equivalent damping ratio is around 2 %. The brown line shows the variation of the amplitude A_2 of the second vibration. The change of this parameter has no influence on the global damping ratio. The yellow line shows the variation of the amplitude A_3 of the third vibration. The calculated equivalent damping ratio slightly increases with increasing amplitude.

All lines show a linear behaviour, although the lines are contradicting at first sight. Increasing A_1 will decrease the calculated equivalent damping ratio, whereas increasing A_3 will decrease the calculated equivalent damping ratio. This can be explained by Eq. (2.14). Since the frequency above the centre-frequency is weighted higher, the calculated equivalent damping ratio is lower. The maximum relative change of the calculated equivalent damping ratio is below 5 %. However, the A_1 parameter has the highest influence, i.e. lower frequencies have higher impact on the calculated equivalent damping ratio.

Damping Ratio: This time the individual damping ratio D_i in Eq. (4.5) of each decaying sine function is varied from 2 % to 3 %. The result is depicted in Fig. 4.5. The relative change of the calculated equivalent damping ratio $\frac{\Delta D_{\text{eq}}}{D_{\text{eq,ref}}}$ is plotted against the relative change of each individual damping ratio $\frac{\Delta D_{\text{i}}}{D_{\text{i,ref}}}$ of each decaying sine function.

The blue line shows the influence of the relative change of D_1 of the first decaying sine function. The calculated equivalent damping ratio is increasing with increasing D_1. The line has a right curvature. In-between jumps of the calculated equivalent damping ratio are observed. The brown line shows the variation of D_2 of the second decaying sine function. This one also shows increasing calculated equivalent damping ratio with increasing individual damping ratio D_2 with a right curvature. The yellow line shows the variation of D_3. The calculated equivalent damping ratio does not change with variation of D_3

All three lines show similar behaviour. The relative change of D_1 leads to the highest relative change of the calculated equivalent damping ratio. The relative change of D_2 still shows a relative change of the calculated equivalent damping ratio, but with less impact than the relative change of D_1. The relative change of D_3 seems to have no impact. Also in this variation the vibration with the lowest frequency has the highest impact. The decay of the higher frequency is covered by the decay of the lower frequencies.

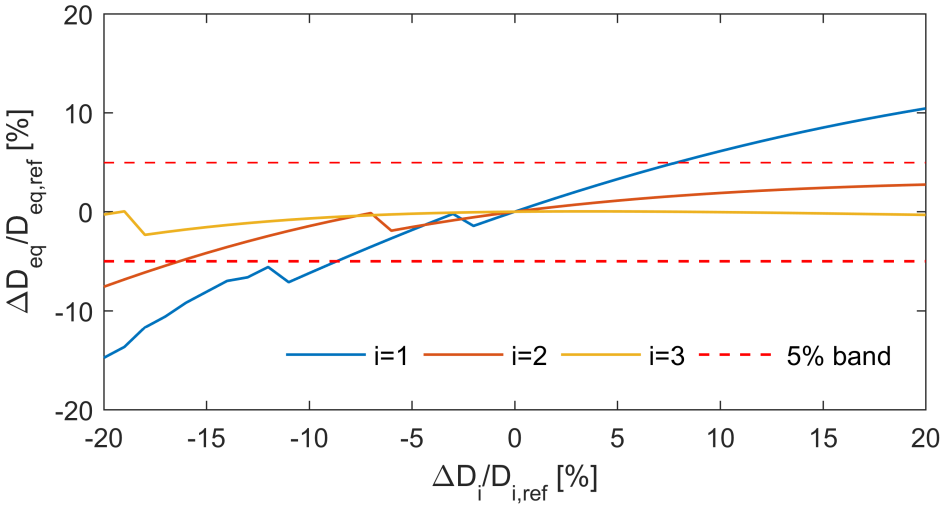

Figure 4.5.: **Variation of the individual damping ratios**

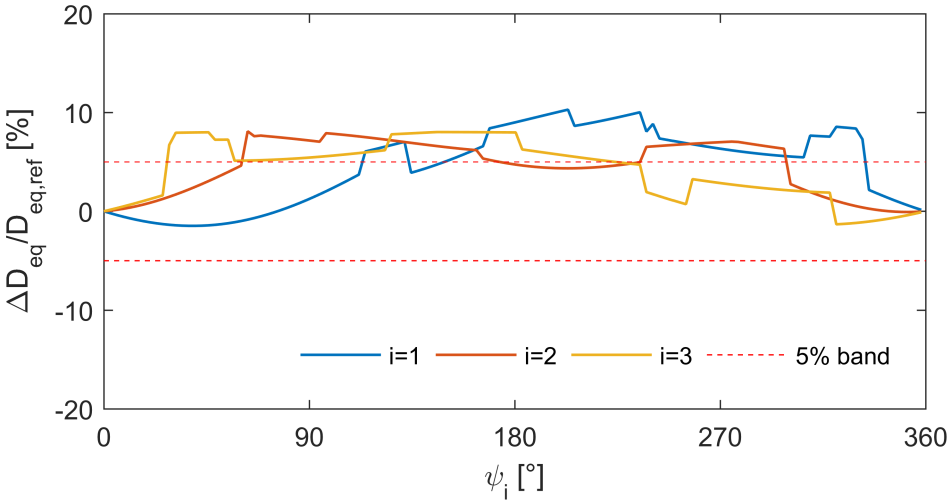

Figure 4.6.: **Variation the phases**

Phase: The phase ψ_i in Eq. (4.5) of each sine function is varied from $0°$ to $360°$ and the calculated equivalent damping ratio is observed. The relative change of the calculated equivalent damping ratio $\frac{\Delta D_{\text{eq}}}{D_{\text{eq,ref}}}$ is plotted against the phase ψ_i in Fig. 4.6.

The blue line shows phase ψ_1 of the first sine function. Up to $90°$ the relative change of the calculated equivalent damping ratio is negative. From $90°$ up to $360°$ the relative change of the calculated equivalent damping ratio is positive. The maximum relative change of the calculated equivalent damping ratio is around $200°$. Due to the periodicity of a sine curve, the relative change of the calculated equivalent damping ratio at $360°$ is $0\,\%$ again. The brown line shows the variation of ψ_2 of the second sine function. The relative change of the calculated equivalent damping ratio is positive for all values of ψ_2. The curve looks like a half sine. The yellow line illustrates the change of ψ_3 of the third sine function. For almost all values of ψ_3 the relative change of the calculated equivalent damping ratio is positive. Around $350°$ the relative change of the calculated equivalent damping ratio is negative.

The relative change of the calculated equivalent damping ratio is oscillating for each variation of the phase shift. All frequencies have the same maximum impact of around $10\,\%$ relative change of the calculated equivalent damping ratio. The calculated equivalent damping ratio can be higher or lower than the reference equivalent damping ratio, depending on the phase shift ψ_i.

Number of Modes: This time the number of vibrations N is varied. So the study is not limited to three sine curves. All parameters stay the same for all decaying sine functions except the frequency. A_i is 1 and ψ_i is $0°$ for all sine functions, D_i is $2.5\,\%$ for all exponential functions. The frequency of each sine function is equally spaced in the analysed frequency band. For instance, with $N = 1$ vibration the frequency f_1 is $200\,\text{Hz}$. For the number of $N = 2$ vibrations, the frequencies are $f_1 = 183.8\,\text{Hz}$ and $f_2 = 216.7\,\text{Hz}$. For $N = 3$ vibrations the frequencies are $f_1 = 175\,\text{Hz}$, $f_2 = 200\,\text{Hz}$ and $f_3 = 225\,\text{Hz}$, respectively. The equivalent damping ratio is calculated for each N from 1 to 100. Figure 4.7 shows the relative change of the calculated equivalent damping ratio versus the number of sine functions within the analysed frequency band. This could also be interpreted as the variation of modal density.

First the calculated equivalent damping ratio is decreasing with increasing number of vibrations. At around 10 vibrations there is a minimum where the reference damping ratio is reduced by more than $50\,\%$. Increasing the number of vibrations further, the calculated equivalent global damping ratio is increasing again. At 20 vibrations the relative change of the calculated equivalent damping ratio is $120\,\%$. With more number

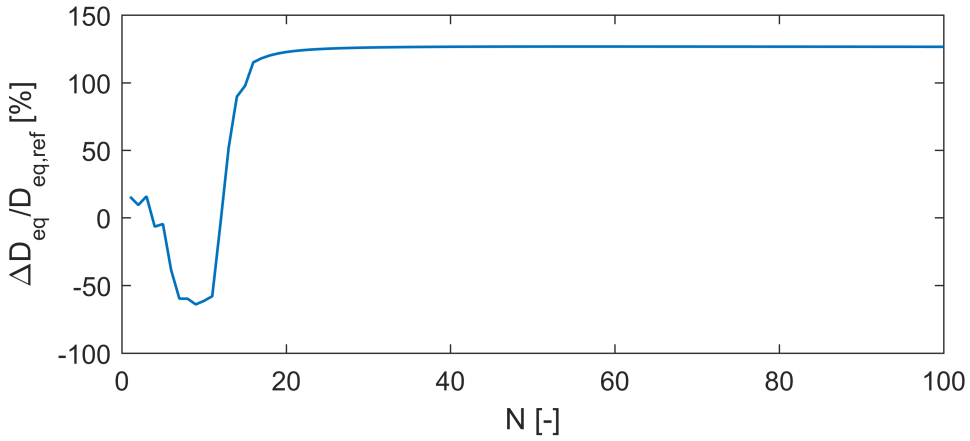

Figure 4.7.: **Variation of the number of vibrations**

of vibrations no further change of the identified damping ratio is observed.

The calculated equivalent damping ratio is highly dependent on the number of vibrations in the analysed frequency band. The calculated equivalent damping ratio is decreasing with increasing number of decaying sine functions. After a critical number of decaying sine functions, the relative change of the identified damping ratio is increasing strongly and converges after $N = 20$ vibrations. A possible reason are the closely spaced frequencies. As already discussed in the impact of the frequency paragraph, closely spaced frequencies can raise the damping ratio dramatically.

Conclusion: The amplitude has a linear influence on the calculated equivalent damping ratio. The amplitude on a structure depends on the mode shape, which varies in space. The phase has a non linear impact. Varying the phase can raise and lower the calculated equivalent damping ratio. Due to the mode shape the initial phase shift can be $0°$ or $180°$. The individual damping ratio of each decaying sine function can have a considerable influence. It is also seen, that the lower frequency dominates the higher one. It is assumed that the damping ratio also varies in space in a real structure. The frequency has a big impact on the relative change of the calculated equivalent damping ratio. However, on a real structure this parameter is fixed and does not vary in space. Also the number of vibrations has a great influence on the calculated equivalent damping ratio. The equivalent damping ratio can be doubled by the number of vibrations. All parameter variations can lead to an underestimated or overestimated equivalent damping ratio. The amplitude, phase and damping ratio are assumed to vary in a real structure. Therefore, it is assumed that the spatial mean value of the calculated

damping ratio according to Eq. (4.3) gives a good estimate for the damping ratio of the structure.

4.2. Application of the Global Damping Identification Method to a Simulation Model

When the spatial mean value of the damping ratio is taken, the local damping ratios become a global damping ratio. This section investigates the number of measurement points needed to obtain a good global damping estimation. The model from Sec. 3.3 with a patch of higher structural damping is taken and the global equivalent damping ratios are calculated in the mid-frequency range, which are compared with the numerical damping ratios obtained by a FE Analysis.

4.2.1. Number of Measurement Points

It is investigated how many points are needed in order to average out the wrongly calculated damping ratios. In the first run, all nodes are taken to calculate the global damping ratio. In the second run every second node is taken. In a third step every third node is taken and so on. In Fig. 4.8 (a) the nodes taken for the first and second run are plotted. The results are shown in Fig. 4.8 (b). The number of measurement points, i.e. number of nodes, and the corresponding calculated global equivalent damping ratio for 6 frequency bands are shown. The centre-frequency is shown in the legend. A logarithmic scale for the x-axis is chosen. The number of measurement points can be reduced dramatically without changing the calculated global damping ratio. It can be seen that the damping ratio does not change after taking around 120 measurement points instead of the maximum number of measured points of 1089. The number of measured points can be reduced to one tenth without a noticeable difference in the calculated damping ratios.

4.2.2. Comparison of Frequency Response Data

In this section the calculated global equivalent damping ratios are compared with the global damping ratios obtained by FE Analysis. Then the calculated global equivalent

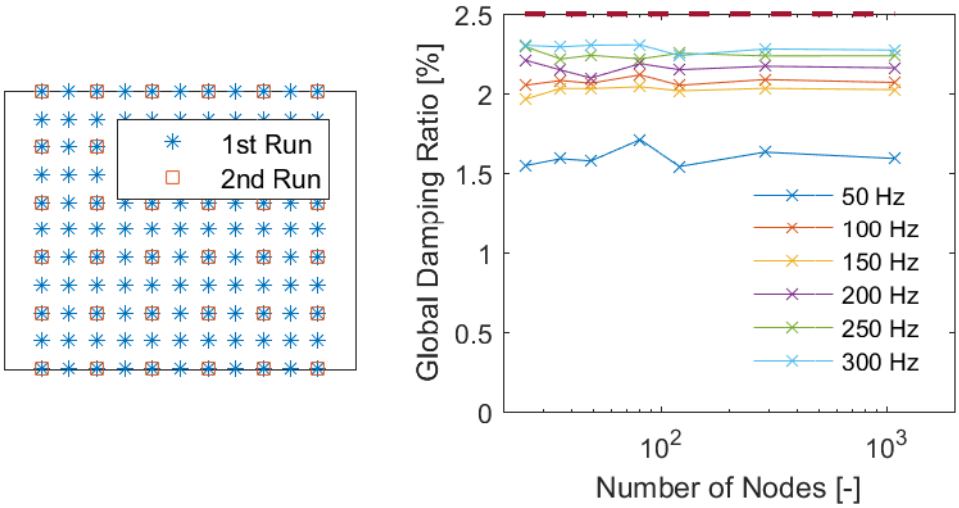

(a) (b)

Figure 4.8.: **Influence of number of measurement points. (a) grid points and (b) calculated damping ratio over varying number of nodes**

damping ratios are applied to the undamped plate described in Sec. 3.1 as modal damping. The FRFs computed from this model are compared with the original FE Model. The process is depicted in Fig. 4.9.

In a numerical complex modal analysis of the FE Model the damping coefficients are computed and compared to the calculated global equivalent damping ratios. The result is shown in Fig. 4.10. The blue crosses are the numerical damping ratios of each eigenfrequency. The red line connects the calculated global equivalent damping ratios at each frequency band. A bandwidth of 50 Hz is chosen. The global equivalent damping ratio for 9 frequency bands are calculated. The centre-frequency is increased from 50 Hz to 500 Hz with a step size of 50 Hz. The analysed frequency bands and the FRF at the driving point is shown in Fig. 4.1. The calculated global equivalent damping ratios are always lower than the numerical values. Comparing this with Fig. 4.7, it means that the modal density is not as high as expected. Since the calculated global equivalent damping ratios are smaller than the numerical values, this is a conservative estimation and well suited for the design process.

In order to compute the estimated FRFs, the undamped plate presented in Sec. 3.1 is used and the calculated global equivalent damping ratios are applied to this model.

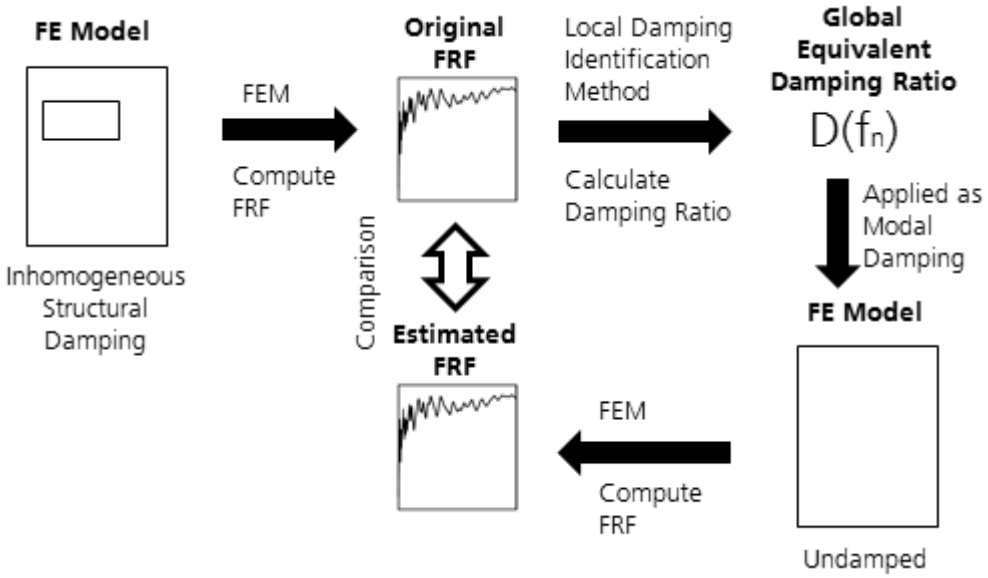

Figure 4.9.: **Procedure to compute estimated FRFs**

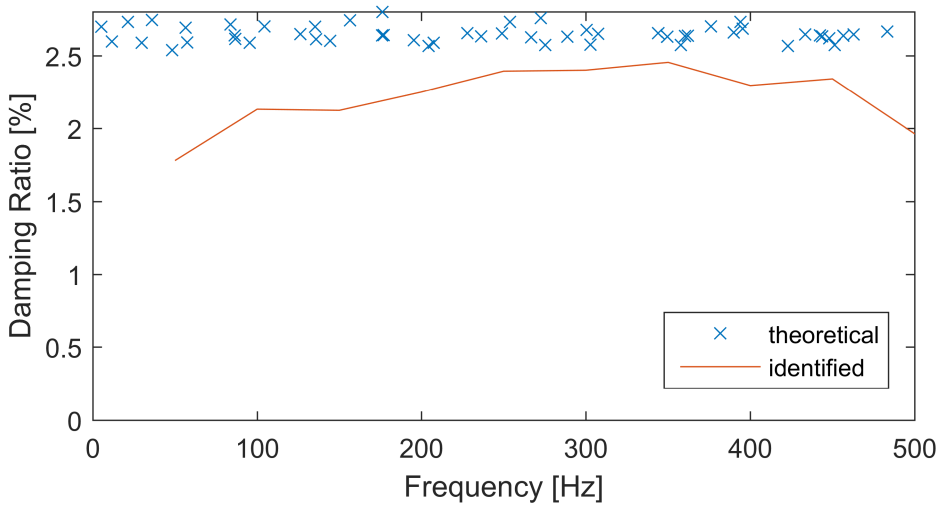

Figure 4.10.: **Comparison of identified and numerical values**

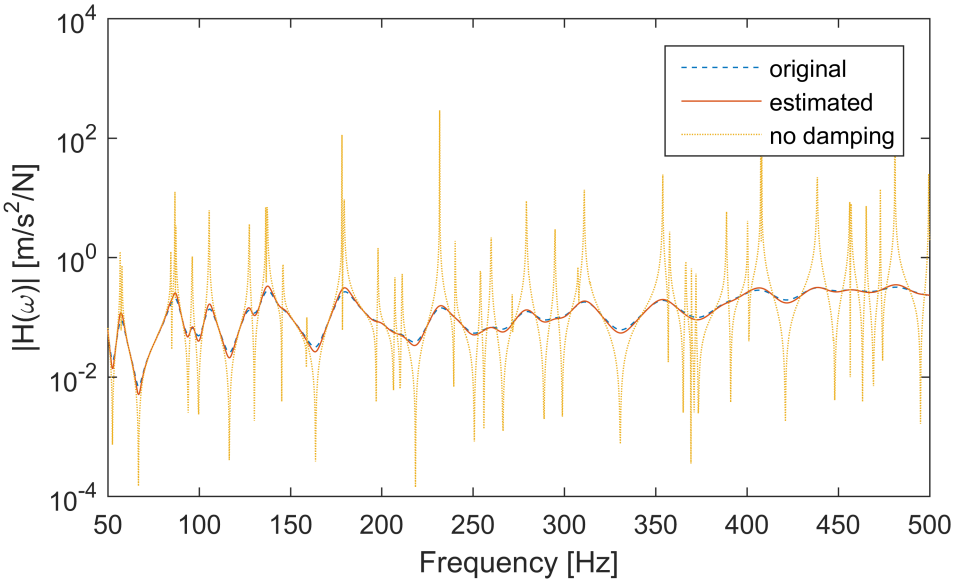

Figure 4.11.: **Comparison of estimated FRF and original FRF**

Modal damping formulated as structural damping is chosen:

$$[H(\Omega)] = \sum_{i}^{N} \frac{\{\varphi\}_i \{\varphi\}_i^{\mathsf{T}}}{\left(\Omega^2 - \omega_i^2\right) - j g_i \omega_i^2}, \tag{4.6}$$

$$\text{with} \qquad g_i = 2D_i, \tag{4.7}$$

where the eigenvector $[\varphi]$ is mass normalised. According to Eq. (4.6) and (4.7), the g_i value is approximated with the calculated global equivalent damping ratios D_i. The corresponding damping ratios for each eigenfrequency is interpolated from Fig. 4.10. This estimated FRF is compared with the original FRF from Sec. 3.3. The comparison between the identified and original FRF is shown in Fig. 4.11. The procedure to calculate this comparison is shown in Fig. 4.9. The red line is the estimated FRF, the blue dashed line is the original FRF. The dotted line shows the FRF without damping. The values at the eigenfrequencies of the no-damping line should be infinity. The shown points are evaluated at discrete points, which are not at the eigenfrequencies, so the amplitude is limited. Figure 4.11 shows that the estimated FRF gives a good approximation of the original FRF, which means that the Method for Local Damping Identification gives a good estimation of the damping ratios in the mid-frequency range.

Figure 4.12 shows the error estimation at each analysed frequency band. The error is

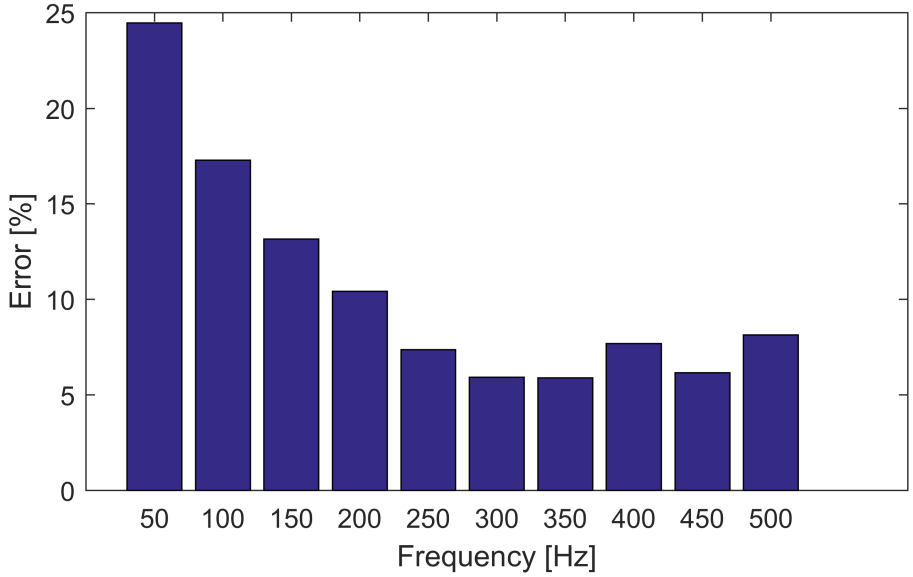

Figure 4.12.: **Error in each frequency band**

calculated as the sum of the differences between the estimated and the original FRF in absolute values in one frequency band with respect to the sum of the original FRF in that frequency band:

$$\varepsilon = \frac{\sum_{f_{\text{band}}} |\text{FRF}_{\text{est}} - \text{FRF}_{\text{orig}}|}{\sum_{f_{\text{band}}} |\text{FRF}_{\text{orig}}|} \tag{4.8}$$

The estimated FRF shows up to 25 % error with respect to the original FRF. The higher the frequency the smaller the error. Also Fig. 4.10 shows that the difference between the calculated global equivalent damping ratio and the numerical damping ratios is decreasing with increasing frequency up to 450 Hz.

The estimated FRF shows a good agreement with the original FRF. Still, it has to be kept in mind that these results are achieved with the correct mass and stiffness matrix. The damping is introduced with a modal approach. As mentioned in the introduction, the eigenfrequencies and the mode shape are not known in the mid- and high-frequency range. So the mass and stiffness matrix is not known. Experiments must show if this approach works with inaccurate mass and stiffness matrix. It has to be tested if these matrices in combination with the identified damping ratios in the mid-frequency range yield good results.

4.3. Conclusion Global Damping Identification in the Mid Frequency Range

The cases in the previous chapter do not validate the local damping identification. The mean value of the calculated damping ratios per frequency band, however, provides a good estimate of the numerical global damping ratio. The analytical test case shows that change in each parameter can lead to an overestimation and underestimation of the theoretical damping ratio. Thus, it is assumed that an average value of the calculated damping ratios provides a good estimation for the damping ratio of the structure. Then, the number of measurement points needed is investigated in order to obtain a good approximation for the calculated global equivalent damping ratio. It is shown that the number of measurement points in this case can be reduced to one tenth without a noticeable difference. Finally an estimated FRF is computed with the calculated equivalent damping ratios, which shows good agreement with the original FRF. The global equivalent damping ratios give a good estimation of the damping ratios in this case.

The EMA methods are applicable in the low-frequency range, but fail in the mid- to high-frequency range. The reviewed method in this thesis is tested on the mid-frequency range. This chapter shows that the calculated global equivalent damping ratios in the mid-frequency range are promising.

5. Conclusion and Outlook

The Method for Local Damping Identification [12] is described and applied to numerical models. The applied damping distribution to the numerical model is compared with the calculated distributions. The calculated damping distributions are not correlating with the applied damping distributions to the FE model.

Chapter 3 describes the calculated damping distributions for three test cases. The damping distributions are identified wrongly due to decay curves affected by beating. Beating occurs when two closely spaced frequencies are present. Also at nodal lines of a mode shape the damping ratio identified is deviating from the theoretical value. Because the decay does not fit to the analysed centre-frequency, the identified damping ratio is wrong. Nevertheless the mean value of each identified damping distribution is close to the theoretical value. These results are obtained by the absence of background noise in the processed signal.

EMA methods are available for low-frequency range applications. In mid- and high-frequency range, however, it is difficult to estimate the correct damping value. The idea of a global equivalent damping ratio is discussed in Ch. 4. The presented Method for Local Damping Identification is tested on global damping values in the mid-frequency range. It is difficult to predict the correct damping ratio in a frequency band if several modes are involved. In mid-frequency range this is inevitable. So an analytical test case was set up to investigate the sensitivity of each parameter of three modes. The parameters have a different effect on the identified global equivalent damping ratio, so the damping ratio is underestimated or overestimated. It is likely that these effects can be averaged out with enough measurement points. It is shown that the number of measurement points can be decreased massively and is still able to average the unwanted effects out for this configuration. Finally, the calculated global equivalent damping ratios are applied to the undamped simulation model and compared with the original simulation model. The estimated FRF and the original FRF are in good agreement, i.e. the calculated damping ratios are in good agreement with the original ones.

The good agreement between the estimated FRF and the numerical FRF has to be

interpreted with caution. The eigenfrequencies and mode shapes are known perfectly, which is not the case in reality. So the numerical results should be validated with a real structure.

The global equivalent damping identification is in good agreement with the numerical global damping ratios of the FE Model. Under the assumptions made in the models in this work, it is not possible to validate the correctness of the calculated damping distributions. Another approach to identify local damping behaviour is model updating. Methods are available to update the damping matrix of FE models. The damping value of each node provides the damping distribution. In SEA the kinetic energy is calculated at each element. Instead of the kinetic energy the dissipated energy could be calculated at each element. The damping distribution might be obtained from the distribution of the dissipated energy.

A. Nastran Interface for Matlab

The usual procedure for FEM consists of three stages: preprocessing, processing and postprocessing. The model setup, like geometry generation, material definition, application of loads and boundary conditions and meshing is part of the preprocessing. Processing is the analysis itself. This step includes the assemblage of the mass and stiffness matrix and the computation of the solution. Postprocessing is the visualisation of the results, for example the modeshapes.

Nastran is only capable of processing. Usually the pre- and postprocessing is done with another application. At the department of Structural Dynamics and System Identification Patran is used. The main tool for data processing in this department is Matlab. A sophisticated in-house Matlab Toolbox (SAS) has been developed for experimental analysis. This toolbox can also visualise data and therefore it is suited for postprocessing results.

Nastran can save the results in op2 file format. An interface in Matlab for op2 files already exists. The SAS Toolbox has several data objects to handle the data. GeomD, for instance, handles geometry data, TimeD handles time domain data and so on. The interface can transfer the Nastran results into these objects, so the data analysis can continue in Matlab.

The SAS Toolbox was extended with an additional object to provide an interface to Nastran. This interface allows preprocessing within the SAS Toolbox.

Nastran needs an input file which contains the mesh data, boundary conditions and loads. The new object is a subclass of GeomD. The mesh data should be already in a GeomD object. It is extended with FEM specific data, like loads and boundary conditions, material properties and so on. This object writes out the Nastran input file and calls a Nastran run in Matlab. It can also return the results from the run.

If the geometry is already provided as a GeomD object, it can be merged into the interface class using the method mergeGeomD(). The element table must have a specific format. The ‘Type’ column contains the finite element type. Right now only ‘CHEXA’ is

supported. The 'Material' column contains the property ID. The element connections must be in the right order. The order for CHEXA elements are provided in the Nastran Quick Reference Manual. The first two rows with each 4 entries are written in this order in the input file.

An example of usage is shown on the next page. In the first line, the interface object is initialised. All result files have the name 'plate_modes' and are stored in D:\Daten\fem. The geometry with the mesh is stored in gdata and is added to the object with the mergeGeomD() method. In this project a function was created to mesh simple plates with the needed properties in the element table.

Line 6 to 14 shows the setup for boundary conditions. In line 8 all rotational degree of freedom are fixed. With the getNodeID method it is possible to get the IDs in a specific range. Node123_1 contains all nodes from 0 to xmax at ymax on the zmax/2 plane. This means the mid layer on the top from left to right. Node123_2 is the bottom line. In line 12 top and bottom of the plate are fixed.

In line 16 the material is set with the ID 1, Young's Modulus of $7 \times 10^{10}\,\mathrm{N\,m^{-2}}$, Poissons ratio of 0.34, density of $2700\,\mathrm{kg\,m^{-3}}$ and structural damping of $5\,\%$.

Line 19 to 27 is the setup of the solver. This has to be done manually. The needed parameters are described in the Nastran Quick Reference Guide. The analysis is started from Matlab and the results are read back in Matlab again.

Listing A.1: **Nastran Interface example**

```
fedata = NastD('plate_modes');
fedata.addPath('D:\Daten\fem');
fedata.mergeGeomD(gdata);

% set boundary conidtions
% fix all rotations
allNodes = fedata.Nodes(:,1);
fedata.addSPC1(1,456,allNodes);
% support top and bottom
Node123_1 = fedata.getNodeID([0 xmax], ymax, zmax/2);
Node123_2 = fedata.getNodeID([0 xmax], 0, zmax/2);
fedata.addSPC1(2,123,[Node123_1; Node123_2]);
% merge both BCs into one ID
fedata.addSPCADD(1,[1 2]);
% set material
fedata.addMat1(1, 7e10, 0.34, 'RHO', 2700, 'GE', 0.05);
fedata.addPSolid(1,1);
% set up solver
fedata.setSolver(103); % Modal Analysis
fedata.addCaseControlRow('ECHOOFF');
fedata.addSubcaseRow(1,'ECHO = NONE');
fedata.addSubcaseRow(1,'SUBTITLE=modal analysis up to 250 Hz');
fedata.addSubcaseRow(1,'METHOD = 1');
fedata.addSubcaseRow(1,'SPC = 1');
fedata.addSubcaseRow(1,'VECTOR(PLOT,SORT1,REAL)=ALL');
fedata.addBulkRow('PARAM   COUPMASS -1');
fedata.addBulkRow('EIGRL,1,0,250,,,,,MASS');
% write Nastran input file
fedata.writeBDF;
% run analysis
fedata.run;
% read results
reader = fedata.getOP2;
gd = reader.write_GeomD;
md = reader.write_ModeD;
md = md.OUG1;
```

List of Figures

List of Tables

Bibliography

[1] ACARE. *European Aeronautics: A Vision for 2020*. Office for Official Publications of the European Communities, 2001.

[2] S. Adhikari. *Damping Models for Structural Vibration*. PhD thesis, University of Cambridge, September 2000.

[3] K.-J. Bathe. *Finite Element Procedures*. Prentice Hall, 1996.

[4] Bruel and Kjaer. Digital filter techniques vs fft techniques. Technical Review 1, 1994.

[5] H. Goyder, D. Lancereau, P. Ind, and D. Brown. Friction and damping associated with bolted joints: results and signal processing. In *ISMA*, International Conference on Noise and Vibration Engineering, pages 755–769. Katholieke Universiteit Leuven, 2016.

[6] C. Hak, R. Wenmaekers, and L. Van Luxemburg. Measuring room impulse responses: Impact of the decay range on derived room acoustic parameters. *Acta Acustica united with Acustica*, 98(6):907–915, 2012.

[7] S. A. Hambric. *Engineering Vibroacoustic Analysis*. Acoustic, Noise and Vibration. Wiley, 2016.

[8] D. Howe. *Aircraft Loading and Structural Layout*. Aerospace series. Professional Engineering Publishing, 2004.

[9] D. Inman. *Engineering Vibration*. Pearson Education, 2009.

[10] MSC Software. *MSC Nastran 2014 Dynamic Analysis User's Guide*, 2014.

[11] D. Newland. *An Introduction to Random Vibrations, Spectral and Wavelet Analysis*. Dover books on engineering. Longman Scientific & Technical, 1993.

[12] M. Norambuena and M. Böswald. A method for local damping identification. In *ECSSMET*, September 2016.

[13] D. F. Pilkey and D. J. Inman. A survey of damping matrix identification. *Engineering Siences & Mechanicss*.

[14] D. Roylance. Engineering viscoelasticity. Technical report, Department of Material Science and Engineering, 2001.

[15] Wikipedia. Beat (acoustics). https://en.wikipedia.org/wiki/Beat_%28acoustics%29 [Accessed 21 February 2017].

[16] R. Winter, M. Norambuena, J. Biedermann, and M. Böswald. Experimental characterization of vibro-acoustic properties of an aircraft fuselage. In *ISMA*, International Conference on Noise and Vibration Engineering, pages 2731–2748. Katholieke Universiteit Leuven, 2014.